Metrologia

Determination of the thermodynamic temperature between 236 K and 430 K from speed of sound measurements in helium

OPEN ACCESS
IOP Publishing
Metrologia

Metrologia **56** (2019) 045006 (25pp)
https://doi.org/10.1088/1681-7575/ab29a2

Determination of the thermodynamic temperature between 236 K and 430 K from speed of sound measurements in helium

R M Gavioso, D Madonna Ripa, P P M Steur, R Dematteis and D Imbraguglio

Istituto Nazionale di Ricerca Metrologica, Strada delle Cacce 91, 10135 Torino, Italy

E-mail: r.gavioso@inrim.it

Received 1 March 2019, revised 6 May 2019
Accepted for publication 13 June 2019
Published 2 July 2019

Abstract

We report speed of sound measurements in helium at 273.16 K and at eight temperatures in the range between 236 K and 430 K. These results determine the difference $(T - T_{90})$ between the thermodynamic temperature T and its approximation T_{90} by the International Temperature Scale of 1990 (ITS-90). The uncertainty of our measurements of $(T - T_{90})$ spans between a minimum of 0.25 mK near 247 K and a maximum of 0.89 mK at the freezing point of indium (429.75 K) with comparable contributions from the uncertainty of our acoustic determination of T and from the uncertainty of our laboratory realization of ITS-90. On the overlapping temperature ranges these results are consistent with other recent acoustic determinations of $(T - T_{90})$. We also present evidence that $(T - T_{90})$ can be determined with comparably small uncertainties by the alternative, time-saving procedure of measuring the speed-of-sound in helium using only a single, judiciously-chosen, pressure on each isotherm.

Keywords: primary thermometry, acoustic gas thermometry, ITS-90

S Supplementary material for this article is available online

(Some figures may appear in colour only in the online journal)

1. Introduction

1.1. Foreword and organization of the manuscript

Following the institution of the International Temperature Scale (ITS-90) [1], the adequacy of the definition of T_{90} in providing an accurate approximation of the thermodynamic temperature T was tested by several primary thermometry methods [2, 3]. Among these methods, acoustic gas thermometry (AGT) [4], dielectric constant gas thermometry (DCGT) [5] and Johnson noise thermometry (JNT) [6] were refined during the last decade and achieved a substantial reduction of the uncertainty in the determination of the Boltzmann constant k with experiments designed to perform best at 273.16 K or over a reduced cryogenic temperature range. These improvements have motivated further work to extend the useful working temperature range of both methods with the aim of providing an accurate estimate of the difference $(T - T_{90})$. The experimental work and the results presented here contribute to this undertaking using AGT in the temperature range approximately comprised between the triple point of mercury and the freezing point of indium.

Recalling the basic principle of AGT, the thermodynamic temperature T and the speed of sound in the limit of zero pressure u_0 are related as:

$$T = \frac{M}{\gamma_0 R} u_0^2 (T), \tag{1}$$

where $R = kN_A$ is the molar gas constant, N_A is the Avogadro constant, M is the molar mass and γ_0 is the heat capacity ratio at zero density. Equation (1) is the basis of absolute AGT and requires an estimate of the ratio M/γ_0. Absolute AGT was

previously used to determine k at $T_{\mathrm{TPW}} = 273.16\,\mathrm{K}$ at various laboratories around the world [7]. Hence, after the oncoming redefinition of the kelvin [8] will fix an exact value of k, a determination of T using absolute AGT near T_{TPW} would reflect the differences among the previous determinations of k from different experiments until those experiments are improved.

More conveniently for primary thermometry, assuming that M and γ_0 do not differ at T and T_{TPW}, the ratio T/T_{TPW} can be determined by relative AGT:

$$\frac{T}{T_{\mathrm{TPW}}} = \frac{u_0^2\,(T)}{{u_0}^2\,(T_{\mathrm{TPW}})}. \tag{2}$$

Equation (2) is a more convenient choice because it eliminates from the determination of T the first order contribution of those systematic errors which affect the determination of u_0^2 but remain otherwise constant as a function of temperature.

In the following, we discuss our determination of the ratio in equation (2) by measurements of the acoustic f_{ac} and average[1] microwave $\langle f_{\mathrm{mw}}\rangle$ resonance frequencies of a spherical copper cavity with internal radius a using an apparatus whose salient features are briefly described in section 2. When the cavity is filled with helium (He) at pressure p and temperature T, the speed of sound $u(p,\,T)$, the internal cavity radius $a(p,\,T)$, and the acoustic and microwave resonance frequencies are linked by the relations:

$$u\,(p,T) = \frac{2\pi f_{\mathrm{ac}}\,(p,T)}{z_{\mathrm{ac}}}a\,(p,T)\,, \tag{3}$$

$$a\,(p,T) = \frac{z_{\mathrm{mw}}}{2\pi\,\langle f_{\mathrm{mw}}\,(p,T)\rangle}\frac{c}{n\,(p,T)}, \tag{4}$$

where z_{ac} and z_{mw} are mode-dependent eigenvalues determined by the geometrical shape of the cavity and hereafter assumed to be constant as a function of temperature (see section 3.1). In equation (4), c is the speed of light in vacuum and $n(p,\,T)$ is the refractive index of helium. By combining equations (2)–(4), we observe that the ratio $u_0^2(T)/u_0^2(T_{\mathrm{TPW}})$, and hence T/T_{TPW}, can be obtained by two alternative operating procedures.

The first procedure requires measurements of acoustic and microwave frequencies at several pressures p_i along two isotherms, at T and T_{TPW}, and their successive extrapolation to the limit of zero pressure

$$\begin{aligned}\frac{T}{T_{\mathrm{TPW}}} &= \frac{u_0^2\,(T)}{{u_0}^2\,(T_{\mathrm{TPW}})} = \lim_{p\to 0}\frac{f_{\mathrm{ac}}^2\,(p_i,T)}{f_{\mathrm{ac}}^2\,(p_i,T_{\mathrm{TPW}})}\frac{f_{\mathrm{mw}}^2\,(p_i,T_{\mathrm{TPW}})}{f_{\mathrm{mw}}^2\,(p_i,T)}\\ &= \frac{a_0^2\,(T)}{a_0^2\,(T_{\mathrm{TPW}})}\lim_{p\to 0}\frac{f_{\mathrm{ac}}^2\,(p_i,T)}{f_{\mathrm{ac}}^2\,(p_i,T_{\mathrm{TPW}})},\end{aligned} \tag{5}$$

where $a_0(T)$ is the internal radius of the evacuated cavity at T.

The second procedure requires measurements of acoustic and microwave frequencies at two thermodynamic states (p_1, T) and (p_{TPW}, T_{TPW}) and the correction of these data to zero pressure to account for the non-ideality of the gas

[1] In this context the brackets '$\langle\ldots\rangle$' denote the average over the components in a microwave multiplet.

Table 1. Recommended $(T - T_{90})$ differences obtained in this work.

T_{90}/K	Isotherms method $(T - T_{90})$/mK
236.6190	-2.43 ± 0.34
247.0000	-2.65 ± 0.25
260.1200	-1.58 ± 0.29
302.9146	3.73 ± 0.33
334.1700	6.57 ± 0.42
362.6000	7.74 ± 0.53
396.2000	8.73 ± 0.82
430.2400	9.44 ± 0.89

Table 2. Comparison of $(T - T_{90})$ differences obtained using two different methods of analysis.

T_{90}/K	Isotherms method $(T - T_{90})$/mK	Single states method $(T - T_{90})$/mK
235.1400	-2.31 ± 0.40	-2.56 ± 0.46
236.6190	-2.43 ± 0.34	-2.47 ± 0.35
247.0000	-2.65 ± 0.25	-2.68 ± 0.29
260.1200	-1.58 ± 0.29	-1.60 ± 0.26
302.9146	3.73 ± 0.33	3.78 ± 0.35
334.1700	6.32 ± 0.42	6.26 ± 0.41
334.1700	6.57 ± 0.42	6.42 ± 0.43
362.6000	7.74 ± 0.53	7.76 ± 0.46
395.9000	8.21 ± 0.65	8.40 ± 0.62
396.2000	8.73 ± 0.82	8.64 ± 0.63
430.2400	9.44 ± 0.89	9.62 ± 0.97

$$\begin{aligned}\frac{T}{T_{\mathrm{TPW}}} &= \frac{{u_0}^2(T)}{{u_0}^2(T_{\mathrm{TPW}})} = \frac{u^2(p_1,T)}{u^2(p_{\mathrm{TPW}},T_{\mathrm{TPW}})}\\ &\quad\frac{\left(1+\beta_{\mathrm{a}}(T_{\mathrm{TPW}})\rho(p_{\mathrm{TPW}},T_{\mathrm{TPW}})+\gamma_{\mathrm{a}}(T_{\mathrm{TPW}})\rho^2(p_{\mathrm{TPW}},T_{\mathrm{TPW}})+\ldots\right)}{\left(1+\beta_{\mathrm{a}}(T)\rho(p_1,T)+\gamma_{\mathrm{a}}(T)\rho^2(p_1,T)+\ldots\right)}\\ &= \frac{a^2(p_1,T)}{a^2(p_{\mathrm{TPW}},T_{\mathrm{TPW}})}\frac{{f_{\mathrm{ac}}}^2(p_1,T)}{{f_{\mathrm{ac}}}^2(p_{\mathrm{TPW}},T_{\mathrm{TPW}})}\\ &\quad\frac{\left(1+\beta_{\mathrm{a}}(T_{\mathrm{TPW}})\rho(p_{\mathrm{TPW}},T_{\mathrm{TPW}})+\gamma_{\mathrm{a}}(T_{\mathrm{TPW}})\rho^2(p_{\mathrm{TPW}},T_{\mathrm{TPW}})+\ldots\right)}{\left(1+\beta_{\mathrm{a}}(T)\rho(p_1,T)+\gamma_{\mathrm{a}}(T)\rho^2(p_1,T)+\ldots\right)},\end{aligned} \tag{6}$$

where $\rho(p,\,T)$ is the gas density and $\beta_{\mathrm{a}}(T)$ and $\gamma_{\mathrm{a}}(T)$ are, respectively, the second and third acoustic virial coefficients. For helium, the latter thermodynamic properties are accurately known, as a function of temperature, from first-principle calculations [9, 10].

Starting from a collected dataset of acoustic and microwave frequencies recorded as a function of pressure along several isotherms, in section 4.3 we discuss our determination of $(T - T_{90})$, and the associated uncertainty budget, using the procedure described by equation (5), which in the following is referred to as *isotherms method*. At each temperature T, this method estimates $u_0^2\,(T)$ as the fitted intercept of the linear function of the pressure:

$$u^2\,(p,T) - A_2\,(T)\,p^2 = u_0^2\,(T) + A_1\,(T)\,p \tag{7}$$

where the slope $A_1 = \gamma_0\beta_{\mathrm{a}}/M$ provides an experimental estimate of $\beta_{\mathrm{a}}(T)$ and the coefficient A_2 is constrained by a theoretical estimate of $\gamma_{\mathrm{a}}(T)$ [10].

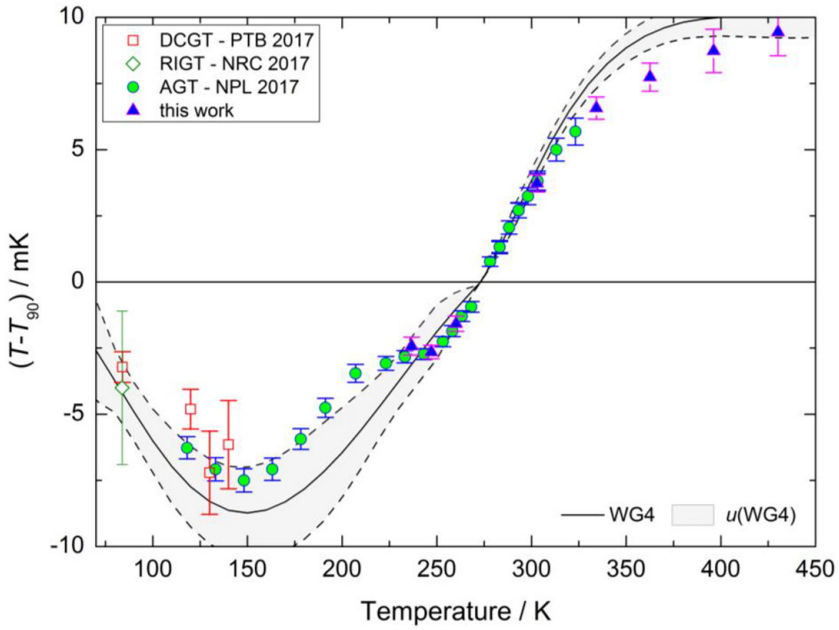

Figure 1. Differences between the thermodynamic temperatures obtained in this work and ITS-90.

In section 4.4 we describe the criteria used for the selection of a subset of the entire collection of acoustic data over a limited pressure range and discuss the alternative determination of $(T - T_{90})$, and the associated uncertainty budget, using the procedure described by equation (6), which in the following is referred to as *single states method*.

The $(T - T_{90})$ results obtained using these two methods are tabulated, plotted and compared with previous estimates in section 1.2.

As evidenced in equations (5) and (6), both methods of analysis require an estimate of the squared thermal expansion of the cavity $a_0^2(T)/a_0^2(T_{\mathrm{TPW}})$ in vacuum, or in helium $a^2(p, T)/a^2(p, T_{\mathrm{TPW}})$, which are obtained from microwave frequency measurements, as discussed in section 3.

The experimental procedures used to test the assumption that the composition of our samples of He does not significantly vary as a function of temperature are described in section 5.

Finally, in section 6 we discuss the instrumentation and the calibration procedures used to link the average temperature of the gas inside the cavity to ITS-90 using capsule-type standard platinum resistance thermometers (cSPRTs), along with the overall uncertainty of our T_{90} estimates.

A more complete list of experimental data, calculated properties, corrections and results than is reported in this paper is available in the form of tabulations or plots as an electronic supplementary section[2].

1.2. Summary of results and uncertainties

Table 1 lists the $(T - T_{90})$ results obtained by extrapolating to zero pressure the speed of sound in He recorded along couples of isotherms, respectively at the unknown thermodynamic temperature T and at 273.16 K.

[2] Electronic supplementary data are available at stacks.iop.org/MET/56/045006/mmedia.

Table 2 compares the $(T - T_{90})$ values determined using two alternative methods of analysis, the *isotherms method* and the *single states method*, discussed in the preceding section. Three additional results listed in table 2, at 235.14 K, 334.17 K and 395.90 K, refer to measurements which were repeated to assess the repeatability of our results against the implementation of some variation of the experimental procedure, like testing the possible effects of outgassing (see section 5). We remark that all the recommended values in table 1 were obtained using the *isotherms method* which, compared to the analysis of single thermodynamic states, is based on a larger experimental dataset and is less affected by our limited capability to model the interaction of the acoustic field in the cavity with the elastic vibration of the shell (see section 4.4). Otherwise, our recommended choice within the multiple $(T - T_{90})$ results obtained for the same, or very near, values of T_{90}, and independently of the type of analysis, is somehow arbitrary, as these results have comparable estimated uncertainties and are found to be all consistent, reinforcing our confidence in their robustness.

1.3. Comparison with recent primary thermometry results

For the temperature range between 70 K and 450 K, figure 1 compares the recommended $(T - T_{90})$ results listed in table 1 with other determinations, by various laboratories and methods, published since 2011. These include the DCGT measurements in He and Ne by the Physikalisch-Technische Bundesanstalt (PTB) [11], the refractive index gas thermometry (RIGT) measurements in He by the National Research Council [12], and the extremely accurate AGT measurements in Ar achieved at the National Physical Laboratory (NPL) [13, 14]. On the same plot, the black line and shaded area display the fitting function and the standard uncertainty of the consensus estimate of previous $(T - T_{90})$ determinations provided in 2011 by a working group (WG4) of the Consultative Committee for Thermometry [2]. Independently of the method, thermometric

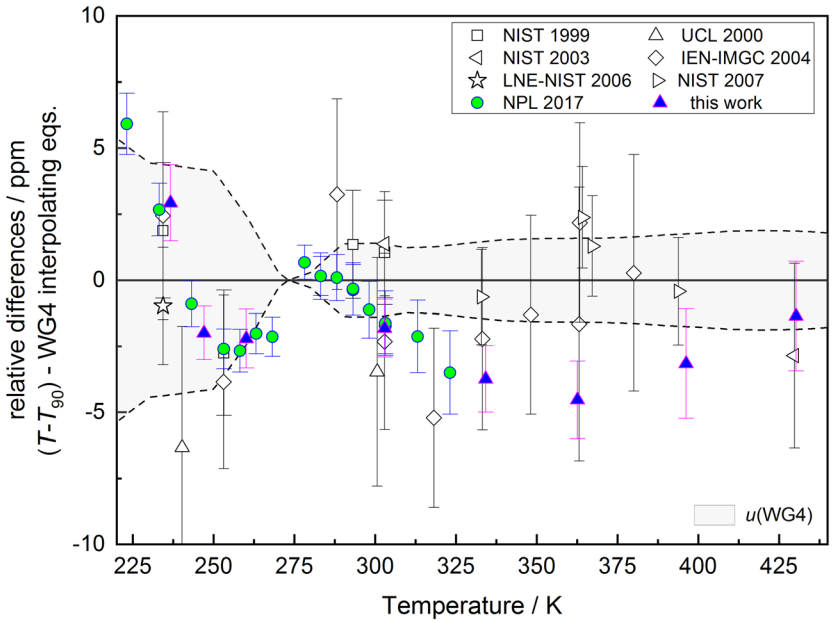

Figure 2. Relative deviations between the thermodynamic temperatures obtained by AGT since 1990 and the interpolating equations of $(T - T_{90})$ worked out by WG4 [2] whose relative uncertainty is plotted as a grey shaded area. Previous AGT results include those obtained at NIST by Moldover *et al* [15], Strouse *et al* [16], Ripple *et al* [17]; at UCL by Ewing and Trusler [18]; at IEN-IMGC by Benedetto *et al* [19]; at LNE and NIST by Pitre *et al* [20]; at NPL by Underwood *et al* [13, 14].

Table 3. Thermostatting fluids used to cover different measuring temperature ranges between 235 K and 430 K.

Temperature range	Main bath	External circulating unit
235 K to 273 K	Ethanol	Ethanol
273 K to 334 K	Water/ethylene glycol mixture	Water
334 K to 430 K	Dow corning xiameter PMX 200[a] silicone oil kinematic viscosity 20 $mm^2\ s^{-1}$ at 25 °C	Julabo thermal HS hydrocarbon mixture

[a] Identification of commercial equipment and materials in this paper does not imply recommendation or endorsement by INRiM nor does it imply that the equipment and materials identified are necessarily the best available for the purpose.

gas and laboratory, all the data in figure 1 are consistent within their combined uncertainty and generally confirm the trend and the statistical significance of the estimated difference between T and T_{90} which had been previously reported [2, 3].

A closer comparison of the two sets of AGT results in figure 1, over their overlapping temperature range, reveals a remarkably close agreement of the trend and values of $(T - T_{90})$ with differences much smaller than the combined uncertainty. As a minor exception to this close match, near the Hg point the difference between NPL determination at 233.15 K and ours at 236.6 K is larger, corresponding to approximately 0.9 times their combined standard deviation. However, the difference of these results reduces considerably, to 0.13 times their combined standard deviation, when they are compared (see figure 2) to the approximation of the thermodynamic temperature defined by the interpolating functions worked out by WG4 [2]. This type of comparison, illustrated in figure 2 between 220 K and 440 K, highlights the remarkable consistency of all the AGT results obtained in this range since the adoption of ITS-90. Considering the most recent NPL and INRiM results, we observe that they fall outside the WG4 estimate in the range between 310 K and 400 K and they both display a significantly different trend of $(T - T_{90})$ around the Hg point, indicating that these data might be useful for a future revision of the WG4 estimate.

2. Synopsis of apparatus and measurement program

In this work we report speed of sound measurements in helium realized using a copper spherical resonator with nominal internal radius of 90 mm and an apparatus comprising an isothermal liquid-bath thermostat and a suitable flow and pressure control manifold. The measurement temperature range spanned between 236 K and 430 K being limited, at the lower end, by the cooling power of the thermostat and, at the higher end, by the presence in the apparatus of a certain amount of polymeric materials and tin-based soldering alloys. Otherwise, the techniques and instrumentation employed in this work could have been used down to a few kelvin, as was previously accomplished by LNE-CNAM and NIST [20], and up to the temperature working limit of the condenser microphones.

The characteristics and the performance of the various components of the apparatus have been previously described in detail elsewhere [21]. With minor exceptions, these instruments were not modified from their original configuration for the period of over two years required to complete data collection spanning between 235 K and 430 K. These exceptions included: replacement of the thermostatting fluids in

Table 4. Calendar and other salient data characterizing the acoustic isotherms.

Date	Isotherm reference temperature K	Notes	Overall pressure range kPa	*Isotherms method* fitted pressure range kPa	*Single states method* selected pressure kPa
02/2014	273.1600		690–60	690–170	350
05/2014	235.1400		690–150		350
05/2014	247.0000		690–170		350
04/2014	260.1200		690–250		350
07/2014	273.1600		690–60	690–170	350
08/2014	236.6190		690–120	600–120	350
07/2014	302.9146		690–105	690–105	350
03/2016	273.1600		690–60	690–180	350
05/2016	334.1700		690–170		380
06/2016	334.1700	After outgassing	690–170		380
06/2016	362.6000		690–170		380
06/2016	395.9000		690–125	690–170	380
07/2016	396.2000	After outgassing	690–170		380
08/2016	430.2400		690–170		380

the main bath, and in the external circulating unit, to suit the measurement temperature range (table 3); adjustment of loop antennas within their holders to improve an effective coupling of microwave triplets (section 3); outgassing of absorbed impurities within the apparatus by heating at 200 °C and the periodic replacement of several source helium bottles (section 5); removal of the cSPRTs for calibration purposes, exchange of their mounting position onto the cavity, and change of the immersion depth of the cavity within the bath to explore possible systematic effects on temperature gradients (section 6).

The measurement program reported here started in February 2014 with the cavity maintained close to 273.16 K. The data collected along this isotherm served as the T_{TPW} reference to determine the ratio T/T_{TPW} from the data of three successive isotherms, respectively at 260 K, 247 K and 235 K. In July 2014, a full isotherm was again recorded near T_{TPW} with the results which led to an accurate determination of the Boltzmann constant [21]; this isotherm data served as a reference to determine T/T_{TPW} at the melting point of gallium (303 K) and to check the repeatability of previous results near the triple point of mercury (236 K). Preliminary comparative plots of these results with other $(T - T_{90})$ determinations achieved by AGT and other methods were anticipated in [2]. Measurements were resumed in March 2016 by recording a third isotherm at 273.16 K, successively used as a reference to determine T/T_{TPW} at four different temperatures, using the data recorded along six isotherms, in the range between 334 K and 430 K. Two of these isotherms (near 334 K and 395 K) were repeated twice, spaced out by the execution of an outgassing procedure, as discussed in section 5, to investigate the possible effect of desorbed impurities. Table 4 summarizes the calendar, pressure and temperature ranges, and a few additional salient data which characterize each single isotherm, including the overall investigated pressure range, and the selected pressure sub-range, or the particular pressure value used to respectively implement the *isotherms method* and the *single states method*.

3. Microwave determination of the thermal expansion of the resonant cavity

An estimate of the internal radius of the resonator $a(p,\ T)$ is needed to convert the measured acoustic frequencies to corresponding values of the speed of sound in helium. As evidenced in equation (4), this estimate can be obtained by measuring the average frequency $\langle f_{\mathrm{mw}}(p,\ T)\rangle$ of the resolved components of a degenerate microwave mode. For our cavity, originally designed and machined to be very nearly spherical in shape, the mode degeneracy was lifted by inducing a slight misalignment upon the initial assembly of its two comprising hemispheres [21].

For the sake of pursuing relative T/T_{TPW} determinations by AGT, the squared thermal expansion of the cavity, i.e. the ratios $a_0^2(T)/a_0^2(T_{\mathrm{TPW}})$ or $a^2(p,\ T)/a^2(p,\ T_{\mathrm{TPW}})$ need to be estimated, as evidenced in equations (5) and (6). With respect to an absolute determination of $a(p,\ T)$, this requirement is more metrologically favorable because it implies that only those frequency perturbations which vary as a function of temperature need to be considered, simplifying the model used to correct the experimental results and reducing the uncertainty budget.

Figure 3 illustrates the validity of this concept in a practical case by displaying the systematic dispersion of $a_0(T)$ which is observed by measuring the frequency of several microwave modes in vacuum at T_{TPW} and at $T = 334.17$ K. To prepare figure 3 the plotted values of the radius were simply prepared by adding together the measured average microwave frequency of each mode and the corresponding average halfwidth $\langle f_{\mathrm{mw}}(p,\ T)\rangle = \langle f_{\mathrm{exp}}(p,\ T)\rangle + \langle g_{\mathrm{exp}}(p,\ T)\rangle$ and using equation (4), where the microwave eigenvalues z_{mw} are those of a geometrically perfect sphere. At both temperatures, the

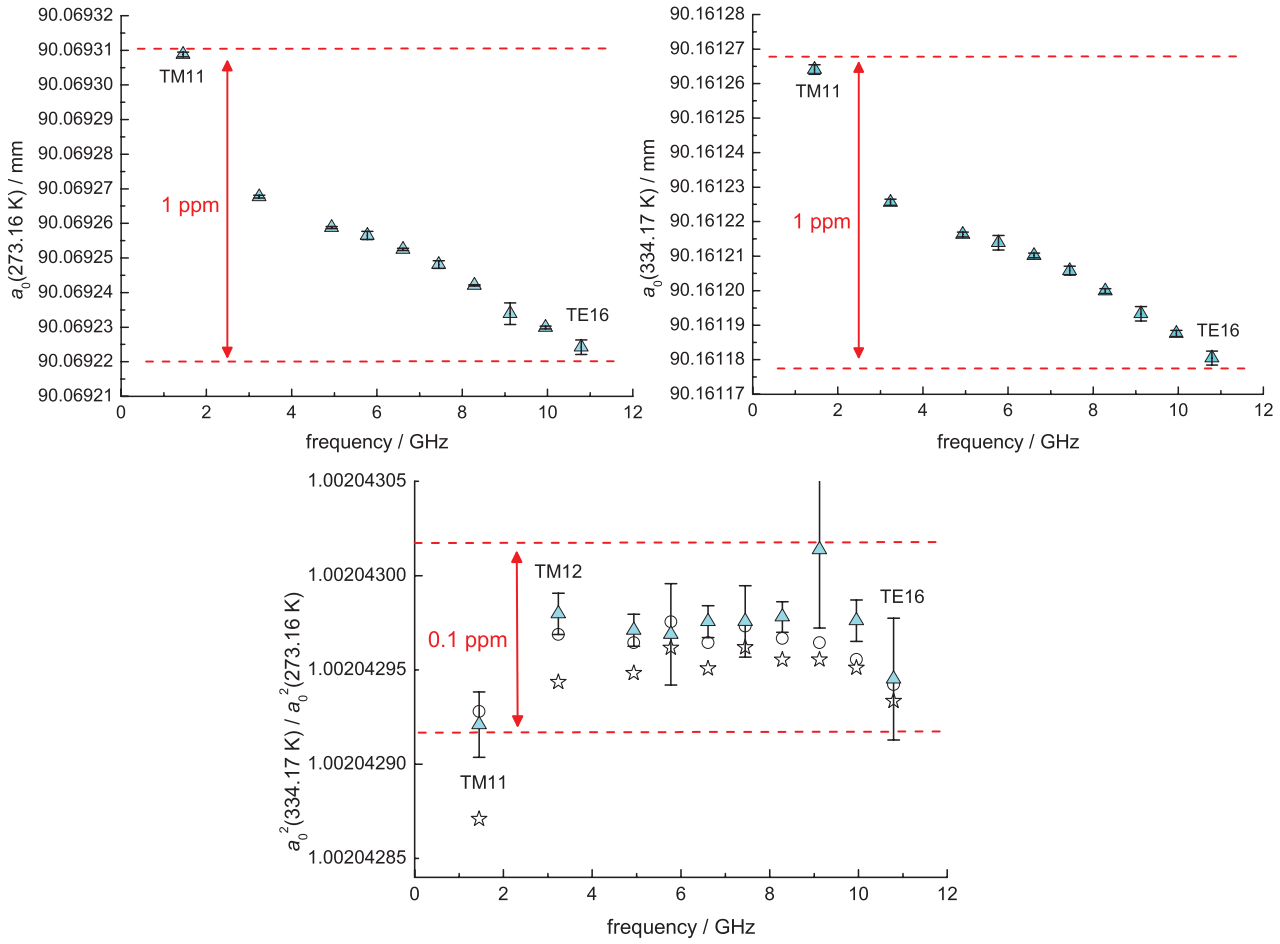

Figure 3. (Upper panel) Microwave radius measured in vacuum at 273.16 K (left plot) and at 334.17 K (right plot) from several microwave modes. At both temperatures, the radii are calculated by simply adding the mode average frequency and the corresponding experimental halfwidth. The uncertainty bars are the standard deviation of repeated measurements for each mode. (Lower panel) squared thermal expansion $a_0^2(334.17\,\mathrm{K})/a_0^2(273.16\,\mathrm{K})$. Full triangles were calculated from the data displayed in the upper panel, i.e. by correcting frequencies using experimental halfwidths. Hollow stars show the slight effect of correcting frequencies using a literature estimate [22] for the resistivity of copper. Hollow circles show the effect of correcting frequencies using our experimental estimate of the surface resistivity and additionally accounting for geometrical imperfections.

systematic dispersion of the radius obtained by different modes reflects the imperfections of this simplified model. However, the plot in the lower panel of figure 3, which displays the squared ratio $a_0^2(T)/a_0^2(T_{\mathrm{TPW}})$, combined from the same data, reduces the relative dispersion of the modes by one order of magnitude. The same plot also shows that $a_0^2(T)/a_0^2(T_{\mathrm{TPW}})$ is only slightly influenced by a more sophisticated perturbation model which takes into account a more reliable estimate of the surface resistivity and the effects of a geometrical perturbation discussed in the following section.

3.1. Microwave frequency measurements and corrections

At each thermodynamic state (p, T) considered in this work, standard instrumentation and procedures [4, 23] were used to repeatedly record and fit the microwave data of several modes. A typical recorded set lasted 12 h and consisted of 30 successive acquisitions of up to 11 triply degenerate modes. At all temperatures, coupling with mode TE11 was too weak to make its recording useful. Occasionally at other temperatures, the resonance data for modes TM12, TE12 and TM16 were excluded from the analysis because of poor coupling and reduced fitting precision of a single peak within the triplet. This problem was enhanced at the highest investigated temperatures by the reduction of the S/N ratio due to the increase of the electrical resistivity of copper. Otherwise, the successively fitted frequencies $\langle f_{\mathrm{exp}}(p_i, T_i)\rangle$ of at least nine modes spanning the frequency range between 1.4 GHz (TM11) and 10.8 GHz (TE16) were first corrected to exact (p, T) values, where p is the mean pressure $\langle p_i\rangle$ of each set, and T is a reference temperature chosen for each isotherm, using equation (8). These corrections compensate for the variation of the resonator radius and the gas density induced by the temperature drifts occurring in the course of the acquisition. Their calculation requires an estimate of the linear thermal expansion coefficient of copper $\alpha_{\mathrm{th}}(T)$ from the literature [24] and a theoretical estimate of the refractive index $n(p, T)$ of He [9, 10, 25–27]:

$$\langle f_{\mathrm{mw}}(p,T)\rangle_i = \langle f_{\mathrm{exp}}(p_i,T_i)\rangle\,[1+\alpha_{\mathrm{th}}(T_i-T)]\,\frac{n(p_i,T_i)}{n(p,T)}. \tag{8}$$

The complete set of repeated acquisitions was then averaged to provide a single estimate $\langle f_{\mathrm{mw}}(p, T)\rangle$ for each mode at pressure p along an isotherm. For each mode, the fit procedure

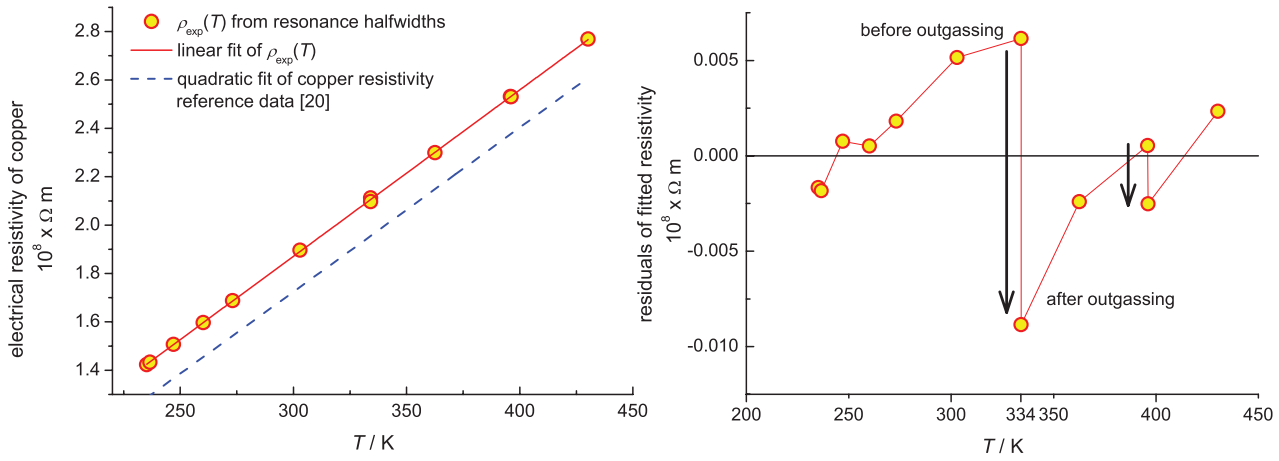

Figure 4. (Left panel) Comparison between the resistivity of copper, experimentally estimated from the resonance halfwidths and a literature estimate [22]. (Right panel) Residuals of a linear fit to our experimental estimated resistivity of copper. At 334 K and 396 K, glitches show the decrease of the resistivity presumably caused by outgassing absorbed impurities on the cavity surface.

separately estimates the halfwidth of each peak within the triplet. Differently from other observations with similar resonant cavities [28, 29], at any temperature or pressure investigated in this work, we did not observe the halfwidth of any singlet peak to significantly differ from the mean halfwidth of the triplet, indicating that the additional energy loss induced by current flow through the equatorial joint was negligible. Thus, for each acquisition we estimated $\langle g_{mw}(p_i,T_i)\rangle$ as the arithmetic mean of the three singlet halfwidths, and the complete set of repeated acquisitions was averaged to provide a single estimate of $\langle g_{mw}(p,\ T)\rangle$ for each mode at each pressure p along an isotherm. The relative standard deviation $u_r(f)$ and $u_r(g)$ of these estimates was typically less than 0.02 ppm and the occasional surpassing of this limit for certain modes was taken as a criterion for data rejection.

Upon preliminary correction using equation (8), and averaging, the frequency data along each isotherm were corrected as $\langle f_{mw}(p,\ T)\rangle + g_{calc}(T)$, where the finite electrical surface resistivity $\rho(T)$ needed to calculate $g_{calc}(T)$ was estimated from the experimental halfwidths $g_{exp}(T)$, revealing a slight frequency dependence previously discussed in [21]. For all modes, and at all temperatures, our estimate of the electrical resistivity $\rho_{exp}(T)$ was larger than its literature reference for pure copper [22] (see figure 4). This difference is partially explained by the increase of the resistivity caused by the steel membrane of two microphones (see section 3.2 in [21]) and to a minor extent by the presence of adsorbed impurities on the internal surface of the cavity or by the inherent impurities in electrolytic though pitch copper (ETP-Cu). The analysis of the residuals of a linear fit of $\rho_{exp}(T)$ as a function of temperature (figure 4), before and after heating the evacuated cavity at 200 °C for the sake of outgassing, reveals a slight systematic decrease in the value of ρ_{exp} which can be ascribed to the effectiveness of impurities desorption or to annealing.

The choice to use our experimental estimate $\rho_{exp}(T)$ or the literature reference $\rho_{ref}(T)$ from [22] for the skin correction of the experimental frequencies has only a minor effect on the determination of $a_0^2(T)/a_0^2(T_{TPW})$, and hence $(T - T_{90})$, as far as $d\rho(T)/dT$ obtained by these two alternative sources is comparable. In fact, from our experimental data we estimate $d\rho_{exp}(T)/dT = (6.88 \pm 0.02) \times 10^{-11}\ \Omega \cdot m \cdot K^{-1}$ which favorably compares with the reference $d\rho_{ref}(T)/dT = (6.79 \pm 0.004) \times 10^{-11}\ \Omega \cdot m \cdot K^{-1}$ fitted to the data in [22]. Conservatively, we assume these small differences as the indicator of a possible temperature-dependent unmodeled energy loss with a corresponding uncertainty contribution to the determination $a_0^2(T)/a_0^2(T_{TPW})$ which is listed in column 3 of table 5.

Table 5. Uncertainty budget for the microwave determination of $a_0^2(T)/a_0^2(T_{TPW})$.

	Relative contribution of different uncertainty sources ppm			
Isotherm temperature K	Mode dispersion	Surface resistivity	Pressure offset	Total ppm
235.1400	0.02	0.01	0.01	0.03
236.6190	0.02	0.01	0.01	0.02
247.0000	0.02	0.01	0.01	0.03
260.1200	0.02	0.00	0.01	0.02
302.9146	0.02	0.01	0.01	0.02
334.1700	0.03	0.02	0.01	0.04
334.1700	0.06	0.06	0.01	0.09
362.6000	0.06	0.05	0.01	0.08
395.9000	0.07	0.06	0.01	0.09
396.2000	0.07	0.07	0.01	0.10
430.2400	0.09	0.07	0.01	0.12

For completeness, but with negligible effect on our estimate of $a_0^2(T)/a_0^2(T_{TPW})$, we corrected our experimental frequency data to account for the deviations of the internal shape of our cavity from perfectly spherical geometry. The effect is negligible because these deviations, as estimated from the relative separation of the peaks within the microwave triplets [30], were not found to vary significantly across the whole temperature range. In fact, if the cavity shape is approximated as an ellipsoid with axes a_0, $a_0(1+\varepsilon_1)$ and $a_0(1+\varepsilon_2)$, the mean estimates $\varepsilon_1 = (1.973 \pm 0.004) \times 10^{-4}$ and $\varepsilon_2 = (1.027 \pm 0.010) \times 10^{-4}$ comprise within one standard deviation the combinations of the geometrical parameters ε_1, ε_2 fitted from the resonance data of all the modes investigated

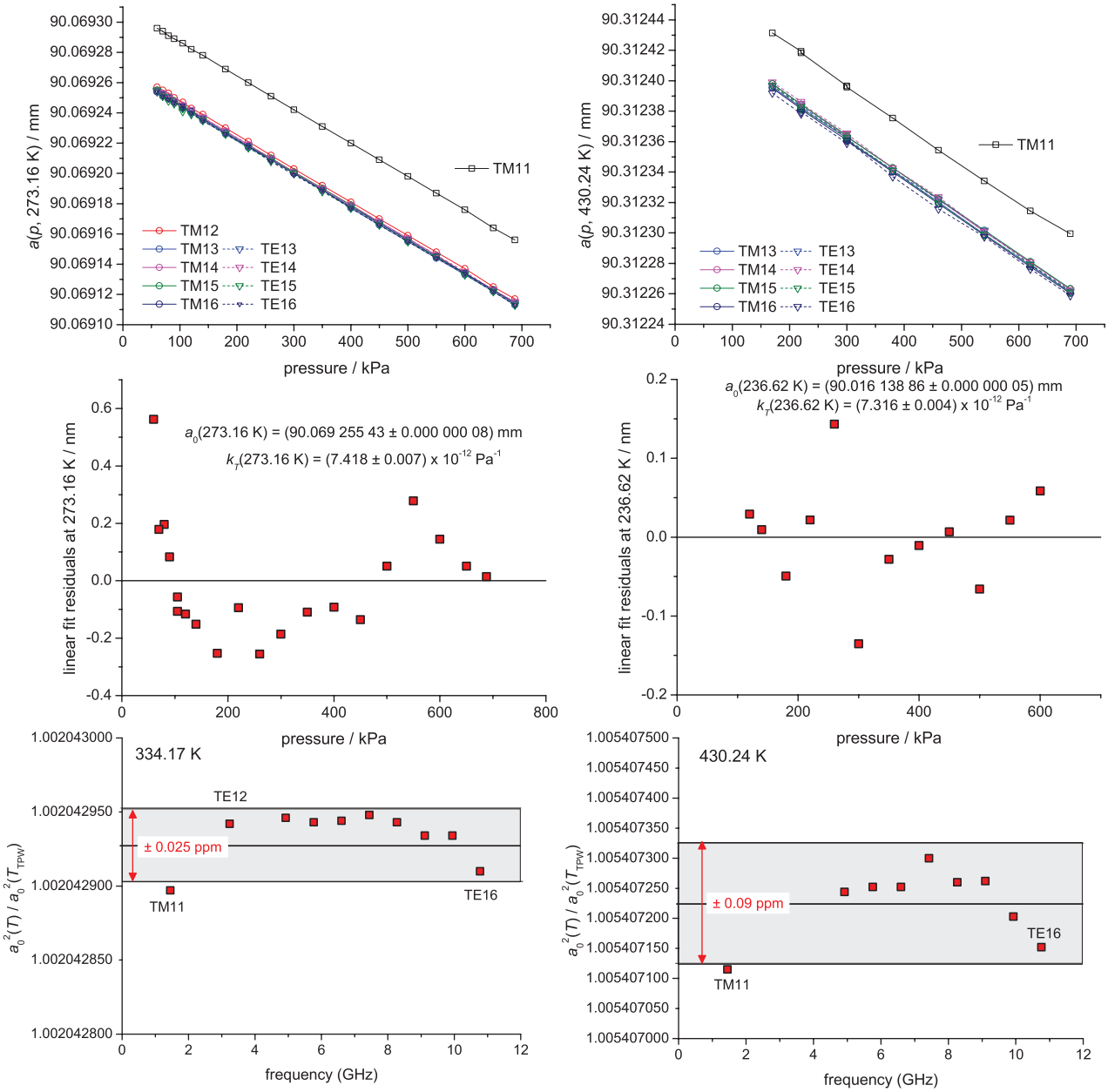

Figure 5. (Upper panel) Cavity radius as a function of pressure from several microwave modes at 273.16 K (left) and 430.24 K (right). (Central panel) Residuals of a linear fit with equation (9) to a mean cavity radius at 273.16 K (left) and 236.62 K (left). The text inset highlights the extraordinary precision of the fitted estimates of the zero-pressure radius $a_0(T)$ and of the effective isothermal compressibility of the cavity $k_T(T)$. (Lower panel) Squared radius ratios $a_0^2(T)/a_0^2(T_{\mathrm{TPW}})$ at 334.17 K (left) and 430.24 K (right). The grey shaded area graphically represents the uncertainty associated to the dispersion of several microwave modes.

in this work (see electronic supplement[3]). Finally, we applied corrections to account for the small perturbations caused by two waveguides backing the antennas and three ducts using the model estimates [31]. Again, the effect of these corrections on our estimate of $a_0^2(T)/a_0^2(T_{\mathrm{TPW}})$ is negligible, as the prediction of these models are not temperature-dependent.

3.2. Estimate of the thermal expansion of the cavity and associated uncertainty

Upon correction for resistivity and other minor perturbations, the microwave frequencies recorded along a single isotherm at temperature T and the refractive index of helium $n(p, T)$ calculated from theory [9, 25–27] provide an estimate, using equation (4), of the elastic variation of the cavity radius as a function of pressure p

$$a\,(p,T) = a_0\,(T)\left(1 - \frac{k_{\mathrm{T}}}{3}p\right) \tag{9}$$

where $k_T = (1/V)(\mathrm{d}V/\mathrm{d}p)$ is the effective volume isothermal compressibility of the cavity. Examples of such variations for different microwave modes and temperatures are plotted in figure 5, showing that the radius calculated from the frequency data of mode TM11 is relatively larger than the average of the other modes by approximately 0.5 ppm. This is

[3] See footnote 2.

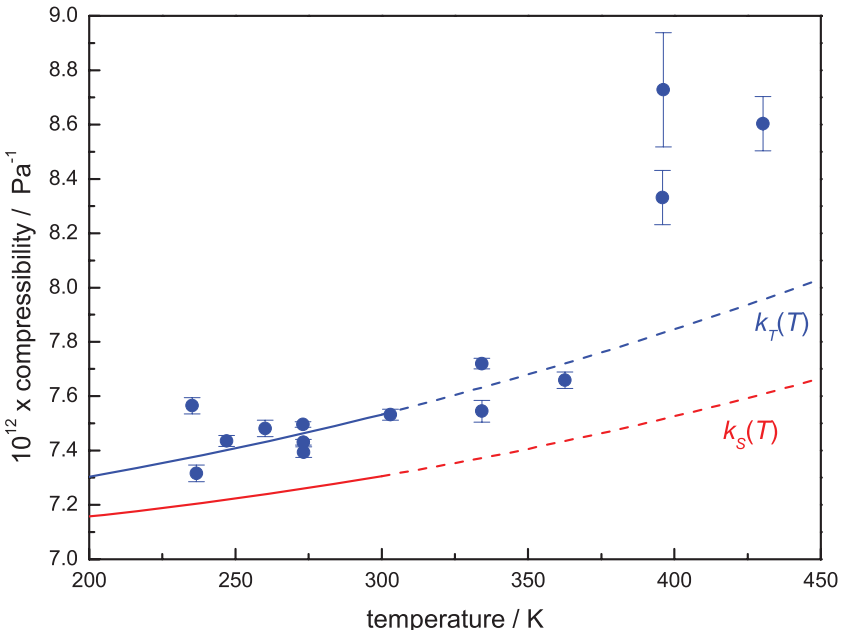

Figure 6. (Full circles) Microwave-based experimental estimates of the effective isothermal compressibility k_T of the resonant cavity. The error bars represent the fitting uncertainty or the discrepancy among different modes, whatever the largest. (Upper blue line) Isothermal compressibility of pure copper k_T based on reference properties of copper [24]. (Lower red line) Adiabatic compressibility of pure copper k_S from the same reference. Dashed lines indicate that the reference estimates from the data in [24] are extrapolated beyond their temperature range of validity.

not surprising, as the peculiarity of the mode TM11 has been a common observation of other AGT experiments [28, 29], and has been previously attributed to the combined perturbing effect of ducts, antenna and microphones.

Along every isotherm, the intercept and the slope of a linear fit to equation (9) respectively estimate the radius at zero pressure $a_0(T)$ and the compressibility $k_T(T)$. We performed these fits separately for each mode N under study (including mode TM11), at temperature T and at T_{TPW}, and combined the results $a_{0N}(T)$ and $a_{0N}(T_{TPW})$ mode by mode to calculate a set of squared ratios $a^2_{0N}(T)/a^2_{0N}(T_{TPW})$. This set was then averaged to provide a single estimate $a^2_0(T)/a^2_0(T_{TPW})$ with an uncertainty contribution tagged as *mode dispersion* in column 2 of table 5 equivalent to half of the relative difference between the values $a^2_{0N}(T)/a^2_{0N}(T_{TPW})$ determined by the most discrepant modes within the set (lower panel in figure 5).

Alternatively, a dataset of $a_{0N}(p, T)$ can be averaged among all modes (including or rejecting TM11 data) and fitted with a linear function of pressure at each temperature. These fits provide extraordinarily precise estimates of $a_0(T)$ (central panel in figure 5). The estimate of $a^2_0(T)/a^2_0(T_{TPW})$ by either procedure discussed above differed less than 0.01 ppm at any temperature.

For the limited number of isotherms where measurements in vacuum were available, a comparison of direct experimental estimates of $a^2_0(T)/a^2_0(T_{TPW})$, with those obtained by the fitting procedures, revealed a maximum relative discrepancy of 0.035 ppm.

For all the isotherms investigated in this work, our estimates of the zero-pressure $a_0(T)$ and $a^2_0(T)/a^2_0(T_{TPW})$, obtained using the procedures and methods discussed above, are included in the electronic supplement[4].

[4] See footnote 2.

Our experimental determinations of the isothermal compressibility $k_T(T)$ are plotted in figure 6, where they are compared with an estimate of the same property from reference data [24] of the adiabatic compressibility k_S using the relationship $k_T = k_S + (9T\alpha^2_{th})/(\rho_{Cu}C_{pCu})$, where ρ_{Cu} and C_{pCu} are, the density and the isobaric heat capacity of copper respectively. The agreement between experiment and prediction is remarkable except at temperatures above 360 K, where the experimental estimate of k_T shows a marked increase. We have no convincing explanation for this increase, but we speculate that it might possibly be caused by annealing. This speculation is seemingly supported by the relative change of 1.1 ppm observed of the cavity radius at 334.17 K (see table S1 in the electronic supplement) after baking the cavity at 200 °C for the sake of outgassing. We do not expect the observed discrepancy in k_T to affect our estimates of T, which are based on zero-pressure extrapolations of the cavity radius. Supporting evidence of this statement comes from the observation that two repeated isotherms near 396 K, respectively measured before and after baking provide consistent estimates of T but inconsistent estimates of k_T.

The overall uncertainty budget of our microwave determination of the (squared) thermal expansion of the resonator $a^2_0(T)/a^2_0(T_{TPW})$ is detailed in table 5. In addition to the contributions due to mode dispersion and surface resistivity previously discussed, we also considered the uncertainty contribution due to our imperfect determination of the gas pressure. The pressure transducer used throughout the course of this work, a quartz sensor with a full-scale range of 690 kPa (Paroscientific 745-100A), was calibrated by comparison with a national reference standard in January 2015. By the results of this calibration, previously reported and commented in section 2.6 of [21], and our long-term experience with this type of

transducer, we conservatively estimate in 20 Pa the maximum systematic undetected drift of the transducer calibration which might occur during the time lapse between measurements at T_{TPW} and at T. To quantify the effect of such possible occurrence in a worst case scenario we applied a constant offset of +10 Pa to our data at T_{TPW} at all pressures and by −10 Pa on our data at T before repeating our analysis based on equations (4) and (9). The resulting effect on our estimates of $a_0^2(T)/a_0^2(T_{TPW})$ is extremely small, relatively less than 0.015 ppm at all temperatures, and is reported in column 4 in table 5 for completeness.

4. Acoustic measurements in helium

4.1. Acquisition and preliminary correction of acoustic data

Using the same instrumentation and procedures described in sections 2.4 and 4.1 of [21], at each pressure step along an isotherm we repeatedly recorded and fitted the acoustic resonance frequencies $f_{(0,N)}$ and the halfwidths $g_{(0,N)}$ of nine purely radial modes, where $N = 2, .., 10$ identifies the mode order. In these records, each successively fitted frequency $f_{(0,N)}(p_i, T_i)$ was corrected to compensate for slight variations of the gas density and the resonator radius induced by temperature and pressure drifts occurring along the record

$$f'_{(0,N)}(p,T) = f_{(0,N)}(p_i,T_i)\,\frac{u(p,T)}{u(p_i,T_i)}\,\frac{a(p_i,T_i)}{a(p,T)}. \quad (10)$$

In equation (10), (p, T) is a single reference thermodynamic state chosen for each record; the prime superscript recalls that $f'_{(0,N)}$ requires further corrections to account for several perturbing effects; $a(p, T)$ is known by the analysis of microwave measurements discussed in section 3; $u(p, T)$ is predicted using the results of the calculations in [9]. We remark that the form of equation (10) corrects a previously published incomplete expression (equation (10) in [21]) by the introduction of the rightmost factor $a(p_i, T_i)/a(p, T)$ whose effect may be relevant if T_i and the reference temperature T differ by more than just a few mK. For each record, the frequencies $f'_{(0,N)}$ obtained using equation (10) and the corresponding halfwidths were averaged to provide a single estimate of $f'_{(0,N)}(p, T)$ and $g_{(0,N)}(p, T)$ for each mode at each pressure p along an isotherm. The relative standard deviation of these average values varies depending on the gas density, the mode order, and the polarization voltage fed to the detector microphone, and typically spans between 0.1 ppm and 1 ppm (full data available in the electronic supplement[5]). These uncertainties were stored and used as weights when fitting to zero pressure a complete set of isotherm data using equation (7).

4.2. Acoustic model

The experimental resonance frequencies $f'_{(0,N)}(p, T)$ differ from their unperturbed values $f_{(0,N)}(p, T)$ because of the interaction of the steady acoustic field with the finite, non-uniform impedance of the internal cavity surface. Such interaction causes the dissipation of acoustic energy as quantified by the resonance halfwidths $g_{(0,N)}(p, T)$. The most relevant effects which are responsible for these perturbations in a spherical resonator were initially modelled by the seminal work of Moldover, Mehl and Greenspan [32] and have recently been the subject of an extensive review [4]. In the following sections, we examine those perturbing effects which, being temperature dependent, are mostly relevant for the sake of an accurate determination of the thermodynamic temperature by relative AGT. To this category do belong the frequency perturbations and the energy losses due to the thermal boundary layer and the coupling of acoustic modes in the cavity with elastic waves in the shell. Perturbations from ducts, microphones and imperfect geometry exhibit only a weak temperature dependence and were included in the model for completeness.

After correcting the raw experimental data to account for all known perturbing effects, the validity of the model can be assessed by two key indicators: (i) the dispersion of speed of sound data around their mean, which is often found to be systematically mode-dependent; (ii) the difference between the experimental resonance halfwidths and the model prediction of the same parameters. Figure 7 shows these indicators as a function of pressure for three isotherms at 236 K, $T_{TPW} = 273.16$ K and 395 K. Plots for the complete set of isotherms examined in this work can be easily reproduced from the data included in the electronic supplement[6].

In figure 7, the plots on the left-hand display the relative difference between the squared speed of sound in He determined from nine radial modes $u^2_{(0,N)}$(p,T) and the function $u^2_{ref}(p, T_{90})$ calculated using reference values of the molar mass of helium M_{He} [33], the molar gas constant R [34][7], and the acoustic virials of helium [9, 10]. At all temperatures, the systematic deviation of u^2 derived from modes (0,2) and (0,3) from the reference u^2_{ref} is evident. Particularly, at 395 K, the mode (0,2) displays a very large deviating trend, relatively spanning between −500 ppm and 800 ppm. These observations highlight our limited capability to account for the coupling of gas resonances and shell motion, particularly for those modes which fall close in frequency to the lowest radial symmetry *breathing* elastic mode of the shell f_{br}. A model of gas-shell interactions, based on the work of Mehl [36], predicts $f_{br}(T)$ to be a slowly variable function of the temperature T spanning between 10.7 kHz at 235 K and 10.1 kHz at 430 K. However, a fitting procedure to our experimental data (see section 4.2.2) provides a rather different estimate of $f_{br}(T)$ which is instead found to vary between 9.4 kHz and 9.0 kHz over the same temperature range, in near coincidence with the experimental frequency of mode (0,2) at 395 K.

For the isotherm at 273.16 K, where the experimental pressure range extends down to 60 kPa, the speed of sound data of modes (0,7), (0,8), (0,9) and (0,10) display anomalous

[5] See footnote 2.

[6] See footnote 2.

[7] The special CODATA 2017 adjustment of the fundamental constants [35] provides a final reference for the value of the Boltzmann constant k and the Avogadro constant N_A; therefrom a conclusive value for R can be derived which differs by only 6 parts in 10^8 from the reference value [34] used in this work.

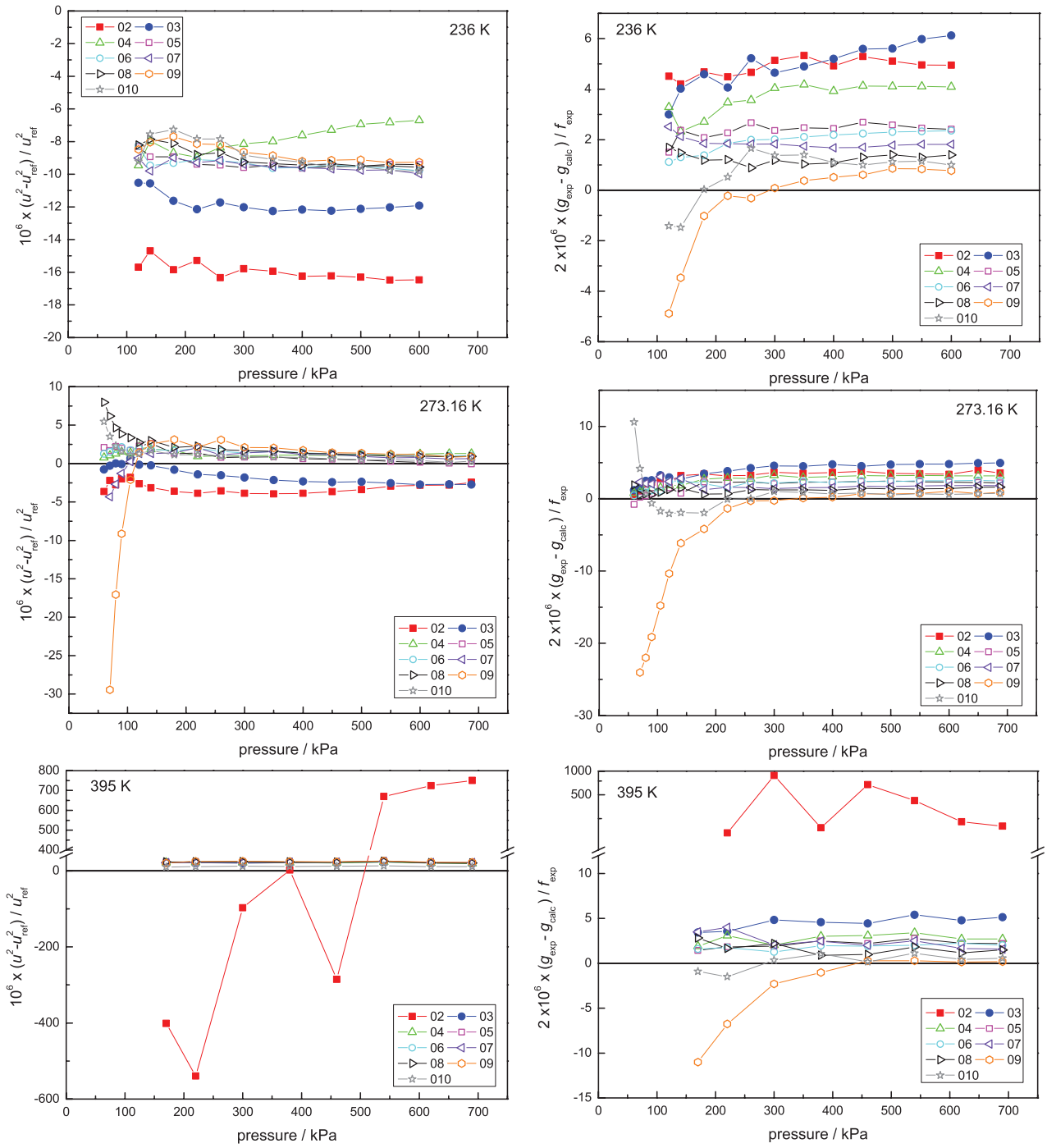

Figure 7. Selected data illustrating the validity of the acoustic model for nine radial acoustic modes at three different temperatures: 236 K, 273.16 K and 395 K. Left plots display the relative deviations of the experimentally determined speed of sound in helium $u^2(p,T)$ from a reference function $u_{ref}^2(p,T_{90})$ calculated from theory [9, 10]. Right plots display the quantities $2 \times 10^6 \times (g_{exp} - g_{calc})/f_{exp}$. Note the scale break on the vertical axis of the bottom plots that highlights the very large perturbation occurring to mode (0,2) near 395 K.

positive or negative diverging trends from the reference. These trends can be interpreted as due to overlapping with neighboring non-radial modes, causing a pressure-dependent perturbation which is hard to predict and is not included in the acoustic model.

The right-hand plots in figure 7 display the resonance excess halfwidths $(g_{exp} - g_{calc})$ multiplied by $2 \times 10^6/f_{exp}$. In good qualitative and quantitative correlation with the deviations shown by the corresponding speed of sound data, the halfwidths of modes (0,2) and (0,3) appear to be anomalously large at all temperatures, while the excess halfwidths of the highest order modes, particularly (0,9) and (0,10), show diverging trends which become increasingly negative at low pressure. Between 180 kPa and 700 kPa, i.e. over the pressure range which has been investigated for all isotherms, the excess halfwidths are found to be approximately constant and their

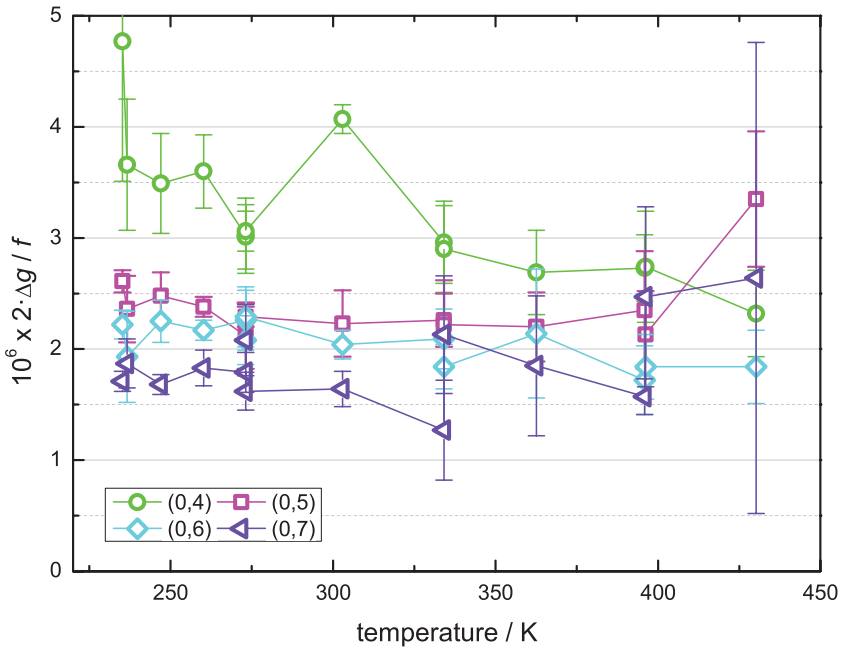

Figure 8. Excess halfwidths $\Delta g = (g_{exp} - g_{calc})$ multiplied by the factor $2 \times 10^6/f_{exp}$ of four radial modes (0,4) to (0,7) as a function of temperature. Each plotted point and error bar represent the mean and the standard deviation of a set of data recorded along an isotherm at pressures between 170 kPa to 700 kPa.

mean value is evidently mode-dependent. Although we have no explanation for these inconsistencies between our model and the experiment, we suspect that they might be caused by an underestimate of the acoustic admittance of the ducts.

Importantly for the sake of accurate primary thermometry, we remark that the observed excess-halfwidths do not significantly vary as a function of temperature. These features are evidenced in figure 8, where the mean values of $2 \times 10^6(g_{exp} - g_{calc})/f_{exp}$, obtained by averaging the data recorded at different pressures, are plotted as a function of temperature, showing that the relative variations of the excess halfwidths when compared at T and T_{TPW} are typically less than ± 0.5 ppm. We account for the few exceptions to this approximate estimate, e.g. the anomalous excess halfwidths of mode (0,4) at 303 K, by a dedicated uncertainty contribution to our determination of $u_0^2(T)/u_0^2(T_{TPW})$, as discussed below in section 4.3.

4.2.1. Thermal corrections. For the purely radial modes in a spherical cavity, the largest perturbation to the resonance eigenfrequencies is caused by the exchange of heat between the gas and the shell which takes place in a narrow layer adjoining the wall. This perturbation scales proportionally to the layer thickness which, at constant pressure and frequency, varies significantly with temperature because of the combined variation of the thermal conductivity and the density of the gas. For helium, these thermophysical properties are so accurately known from theory [9, 10] that their uncertainty contribution to our determination of T/T_{TPW} is negligible, at the relative level of 0.02 ppm or less, even considering the inherent approximation of our laboratory realizations of pressure and temperature [21]. Smaller frequency corrections and/or contributions to the halfwidth account for the propagation of a thermo-elastic wave into the shell, second-order boundary layer theory [37] and for thermo-viscous energy losses in the bulk of the gas. Again, the uncertainty contribution to the determination of T/T_{TPW} due to the imperfect knowledge of the properties of He needed for the calculation of these corrections is negligible.

Instead, a relevant contribution to the overall uncertainty is given by the imperfect estimate of the temperature-jump coefficient ζ_T which is needed to account for the temperature difference at the gas-shell interface [38].

We used a modified version of equation (7), which includes a term inversely proportional to pressure

$$u^2(p,T) - A_2(T)\,p^2 = A_{-1}(T)\,p^{-1} + u_0^2(T) + A_1(T)\,p, \tag{11}$$

to estimate ζ_T for each investigated isotherm from the values of A_{-1} obtained by fitting the acoustic data of modes (0,4), (0,5) and (0,6), which are most reliable at low pressure.

Within the modest evidence brought by their rather large uncertainty, as displayed in figure 9, the fitted values of ζ_T do not show any regular trend as a function of temperature, suggesting that a single average estimate of ζ_T would be valid over the whole investigated range. Two inconsistent determinations of ζ_T resulted from the repetition of acoustic measurements near 395 K before and after baking the resonator at 200 °C under vacuum. The large decrease of ζ_T after baking perhaps indicates a change of the condition of the metal wall, as that which might be caused by the removal of an absorbed surface layer of some contaminant. Based on a handful of more accurate determinations at T_{TPW} and 334 K, we thus assumed $\zeta_T = (6.67 \pm 0.42)$ where the reported value corresponds to the weighted arithmetic mean of the full set of data in figure 9, and the reported uncertainty is obtained by conservatively inflating by a factor of 10 the standard error of the weighted mean, to more realistically represent the dispersion of the full dataset. The corresponding uncertainty contribution

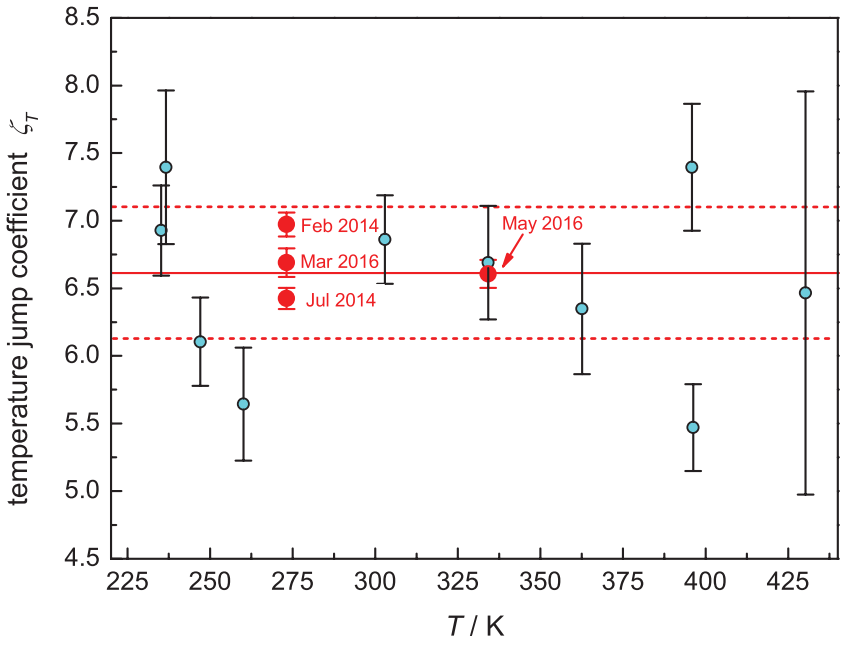

Figure 9. Estimates of the temperature jump coefficient ζ_T for He in contact with copper at different temperatures between 236 K and 430 K. At each temperature, the uncertainty bar encompasses the discrepancies of the estimates of ζ_T from different acoustic modes. Red full symbols and text labels highlight the most accurate estimates obtained by acoustic data recorded over an extended pressure range along three isotherms at T_w and one isotherm at 334 K. The red lines graphically represent the mean value and the uncertainty of our overall temperature-independent estimate $\zeta_T = 6.67 \pm 0.42$.

to the determination of the thermodynamic temperature using the *isotherms method* or the *single states method* are respectively discussed below in sections 4.3 and 4.4.

4.2.2. Shell coupling. Coupling of the acoustic field within the cavity with elastic vibrations in the metallic resonator structure represents a major source of perturbation. The theoretical model first developed by Mehl [36] allows a calculation of the *breathing* shell frequency f_{br}, i.e. the lowest order extensional mode, based on the simplifying assumption that the resonator structure is an isotropic spherical shell. Previous experimental investigations of the validity of this assumption [39, 40] were only partially successful and time consuming, and thus unpractical to be implemented for this work; however, these previous attempts evidenced that the elastic response of a resonator comprised of two bolted hemispheres may differ significantly from that predicted by the analytical model [36], revealing the influence of multiple shell resonances with relevant complex eigenfrequency perturbations. Also, the shell perturbations are expected to vary significantly with temperature because of the combined variation of the acoustic impedance of the gas and, to a minor extent, of the compressibility of the shell. In spite of these limits and complications, we used the full set of recorded acoustic data for nine modes (0,2) to (0,10) to determine by fitting, separately for each investigated isotherm at temperature T_i, the combination of gas and shell parameters $\beta_a(T_i)$, $f_{br}(T_i)$, $\chi_S(T_i)$ which best defines the linear term $A_1(T_i)$ in the acoustic virial expansion (equation (7))

$$\frac{A_1(T_i)}{{u_0}^2} = -\frac{2}{3}\frac{\gamma_0 \chi_S(T_i)}{\left[1-\left(\frac{f}{f_{br}(T_i)}\right)^2\right]} + \frac{\beta_a(T_i)}{RT}. \qquad (12)$$

In equation (12), the estimates of $A_1(T_i)$ have been previously obtained by linear fits using equation (7), and $\chi_S(T)$ is the adiabatic compressibility of the shell [41] which accounts for the compliance of the shell induced by the internal acoustic pressure:

$$\chi_S(T) = \frac{3}{a}\frac{\partial a}{\partial p} = \frac{3}{Y(T)}\left[\frac{1-\nu(T)\left(b^3+2a^3\right)}{2\left(b^3-a^3\right)} + \nu(T)\right], \qquad (13)$$

where a and b are the internal and external radius of the cavity, and $Y(T)$, $\nu(T)$ are the Young's modulus and the Poisson ratio of copper, respectively.

Figure 10 shows the remarkable overall agreement of our acoustic data with the simplified model defined by equations (12) and (13), and evidences the transition of mode (0,2) across a large shell perturbation around 9.2 kHz, taking place at some intermediate temperature between the investigated isotherms at 362 K and 395 K.

In figure 11 we compare the expected temperature variation of $f_{br}(T)$ and $\chi_S(T)$, calculated using equation (30) in [36] and the model equation (13) with tabulated values of the elastic properties of copper [24][8], with the estimates $f_{br}(T_i)$ and $\chi_S(T_i)$ obtained by fitting acoustic data to equation (12). From the comparison, we observe that in spite of the systematic offset between calculated and fitted properties, the trend of both $f_{br}(T)$ and $\chi_S(T)$ were found to be in reasonable agreement. Also, the data in figure 11 show that the relevant shell parameters are stable as a function of time, with three closely

[8] Only measurements based upon dynamic methods were considered in [25]. These methods determine the adiabatic rather than the isothermal elastic moduli.

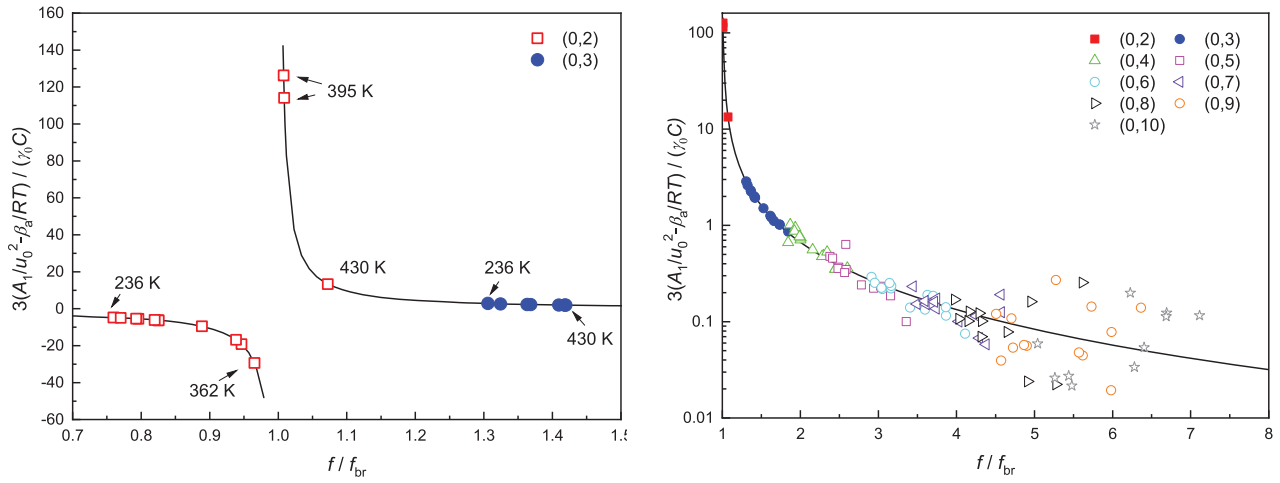

Figure 10. Coupling of radial acoustic modes excited within the resonator with elastic vibrations of its structure between 236 K and 430 K. The black line represents the function $-2/(1-x^2)$ which has the same form as the perturbation model in equation (12) with $x = f/f_{br}$. For each investigated isotherm at temperature T_i the experimental acoustic data are first used to fit $A_1(T_i)$ using equation (7) and, successively, to fit $\beta_a(T_i), f_{br}(T_i), \chi_S(T_i)$ using equation (12). For each mode at each temperature, the plotted symbols represent the fitted results combined as $3[A_1(T_i)/u_0^2(T_i) - \beta_a(T_i)/R\,T_i]/[\gamma_0\chi_S(T_i)]$ as a function of $f/f_{br}(T_i)$.

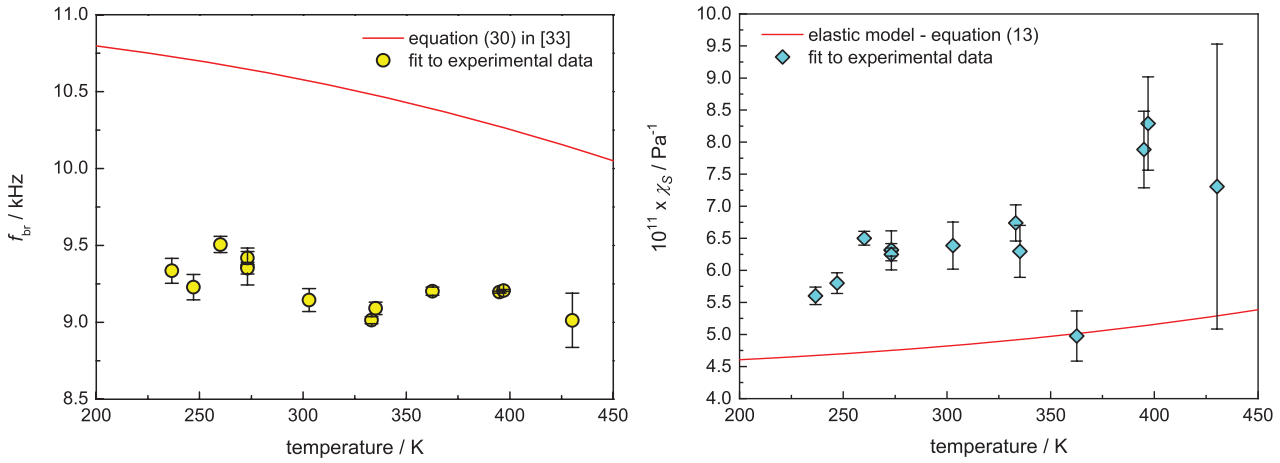

Figure 11. Comparison of the *breathing* frequency $f_{br}(T)$ and the adiabatic compressibility of the shell $\chi_S(T)$ as determined by reference models [36, 41] (red solid lines) or by fitting experimental acoustic data using equation (12). The error bars display the statistical uncertainty of the fitting procedure.

matching estimates of $f_{br}(T_{TPW})$ over a period of nearly 2.5 years and, for repeated isotherms at 334 K and 395 K, in spite of baking the cavity with thermal cycles up to 480 K.

Finally, in figure 12, we compare the values of the second virial coefficient $\beta_a(T_i)$ of He, fitted by equation (12), with the theoretical prediction of the same quantities from a recent first-principle calculation [9], finding these estimates in satisfactory agreement.

4.2.3. Corrections from ducts, microphones, geometry. The uniformity of the acoustic admittance of the internal cavity surface is interrupted by the opening of three ducts respectively used to flow gas into and out of the cavity and to connect the cavity interior to the pressure transducer, and by the front diaphragm of two ¼″ condenser microphones used to drive and detect acoustic signals.

The ducts are designed to be sufficiently long and narrow (see [21] for dimensional details) that their overall acoustic impedance is dominated by the geometry of their initial section and only minorly affected by the terminal impedance of their final section which, being exposed to room temperature, may be sensitive to changes in the temperature profile along the duct. The methods illustrated in [42] were used to calculate the complex acoustic impedance of the ducts. The corresponding relative frequency perturbations were always less than 0.5 ppm for all the modes and at all the temperatures and pressures explored in this work. Importantly, for any given mode and pressure, the relative variation of the perturbation induced by temperature changes between 235 K and 430 K was always less than 0.01 ppm, indicating that neglecting duct corrections would have a negligible impact on the determination of the thermodynamic temperature using the relative method implemented in this work.

Similar considerations hold for the perturbations induced by the acoustic transducers, which were calculated at all temperatures using the models and the methods discussed

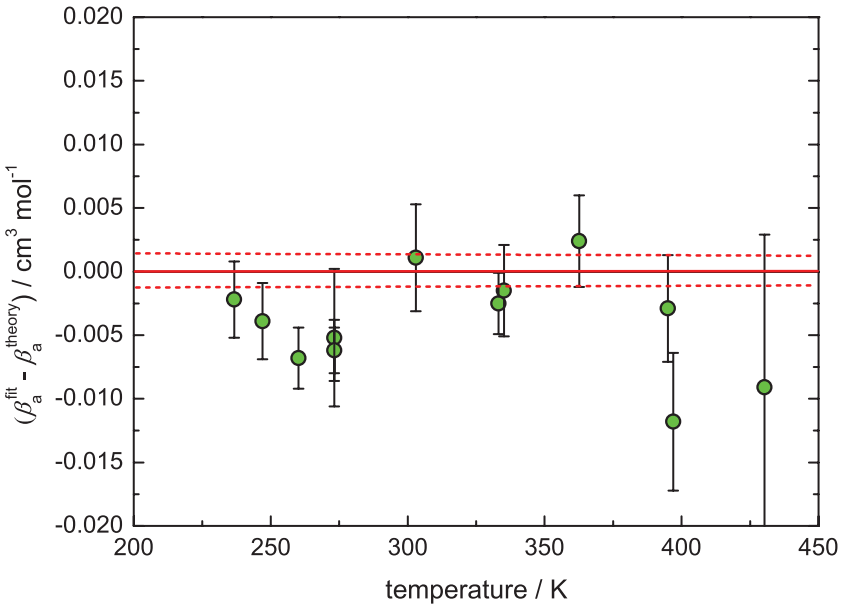

Figure 12. Comparison between the second acoustic virial coefficients β_a of He determined in this work (circles) and their accurate prediction from a recent first-principle [9] (red solid line). The error bars display the fitting uncertainty. The dashed lines delimit the uncertainty of the calculation.

in [43]. These perturbations are always relatively less than 1 ppm, and show minor variations as a function of temperature, typically less than 0.1 ppm.

Finally, as anticipated in section 3.1, over the whole investigated temperature range the observed change of the deformation parameters ε_1, ε_2 were so small to result in barely significant variations, relatively less than 0.01 ppm, of the microwave eigenvalues.

Only for the sake of completeness, we included the effects of ducts, microphones and geometry in our model and calculated and applied the corresponding corrections to the experimentally recorded acoustic data. Again we remark that the alternative choice to simply disregard these effects would have a negligible effect on our determinations of the thermodynamic temperature and their uncertainty.

4.3. Isotherms method: results and uncertainty budget

We now discuss the relevant contributions, listed in table 6 below, to the uncertainty of our determination of the thermodynamic temperature $T/T_{TPW} = u_0^2(T)/u_0^2(T_{TPW})$ when both terms in this ratio are determined by linear fits of acoustic data recorded along isotherms using equation (7).

We first consider the imperfect validity and the incompleteness of the acoustic model, discussed in section 4.2, which suggested the selection of a subset of acoustic modes and a limited pressure range as the most reliable for the determination of the thermodynamic temperature. Recalling the rationale of this choice, modes (0,2) and (0,3) were excluded because, falling close to the shell *breathing* frequency, they undergo large, hardly-predictable perturbations. The high-order modes (0,8), (0,9) and (0,10) were also excluded because they are systematically perturbed by overlapping with neighboring modes, especially at low pressure.

Where available, low pressure data were used to estimate the temperature jump coefficient $\zeta_T = (6.67 \pm 0.42)$ using equation (11) but these data were not included in the final regression of the isotherms to maintain the uncertainty contribution of the imperfect estimate of ζ_T within acceptable limits. Thus, the final selection included four radial modes (0,4), (0,5), (0,6), (0,7) over a pressure range typically spanning between 170 kPa and 700 kPa (see table 4 for details).

Squared speed of sound data were prepared for analysis starting from the measured acoustic frequencies, adjusting to reference mean values of pressure and temperature as described by equation (10), applying the corrections predicted by the model discussed in the previous section, using the microwave estimate of the squared cavity radius $a^2(p,T)$ and, finally, by subtracting the p^2 term which is proportional to the calculated 3rd acoustic virial coefficient of He [9].

These acoustic data were then fitted to the linear function of pressure, equation (7), to estimate zero-pressure intercepts $u_0^2(T)_N$ and slopes $A_1(T)_N$ separately for each mode (0, N). Typical results for the complete set of nine radial modes ($N = 2, .. 10$) are displayed in figure 13 for two isotherms at 273.16 K and 362.60 K, showing a mode-dependent systematic dispersion which reveals the imperfectness of the acoustic model. For each isotherm, a single collective estimate $u_0^2(T)$ was then determined as the weighted mean of $u_0^2(T)_N$, for the selected modes ($N = 4, .. 7$), with weights corresponding to the fitting uncertainty of the isotherm data of each mode. Looking for a proper estimator of the uncertainty of $u_0^2(T)$ we ruled out the standard error of the weighted mean which, by definition, would not account for mode inconsistencies, such as those clearly evidenced in figure 13. Instead, we conservatively assumed that one half of the largest difference between the estimates $u_0^2(T)_N$ would be a more realistic indicator of the mode-dependent uncertainty of $u_0^2(T)$. This is the contribution to the overall uncertainty of $u_0^2(T)/u_0^2(T_{TPW})$ which is listed

Table 6. Uncertainty budget for the determination of the thermodynamic temperature $T = 273.16 \times u_0^2(T)/u_0^2(T_{\mathrm{TPW}})$—*isotherms* method.

Date T isotherm		May 2014	Aug 2014	May 2014	Apr 2014	Jul 2014	May 2016	Jun 2016	Jun 2016	Jun 2016	Aug 2016	Aug 2016
Reference TPW isotherm		I Feb 2014	II Jul 2014	I Feb 2014	I Feb 2014	II Jul 2014	III Mar 2016	III Mar 2016	III Mar 2016	III Mar 2016	III Mar 2016	III Mar 2016
Isotherm temperature/K		235.14	236.62	247.00	260.12	302.91	334.17	334.17	362.60	395.90	396.20	430.00
Row	Uncertainty source	Relative uncertainty $u_{\mathrm{r}}(T)$/ppm										
1	Mode inconsistency at T	0.63	0.43	0.44	0.79	0.29	0.64	0.44	0.66	0.74	1.32	1.15
2	Mode inconsistency at T_{TPW}	0.40	0.56	0.40	0.40	0.56	0.64	0.64	0.64	0.64	0.64	0.64
3	Excess halfwidth variation between T and T_{TPW}	0.53	0.09	0.17	0.20	0.16	0.14	0.01	0.05	0.16	0.04	0.24
4	Thermal accommodation	0.06	0.03	0.05	0.05	0.34	0.35	0.55	0.63	0.63	0.63	0.62
5	Pressure error	0.22	0.21	0.21	0.20	0.19	0.18	0.18	0.17	0.16	0.16	0.15
6	Thermal expansion microwave determination	0.03	0.02	0.03	0.02	0.02	0.04	0.09	0.08	0.09	0.10	0.12
7	Molar mass	0.33	0.35	0.33	0.33	0.00	0.05	0.05	0.05	0.05	0.05	0.14
	Combined/ppm	**1.00**	**0.82**	**0.73**	**0.99**	**0.76**	**1.00**	**0.97**	**1.13**	**1.19**	**1.61**	**1.49**
		Relative uncertainty $u_{\mathrm{r}}(T)$/Mk										
	Combined/mK	**0.24**	**0.21**	**0.19**	**0.26**	**0.22**	**0.31**	**0.30**	**0.38**	**0.43**	**0.61**	**0.61**

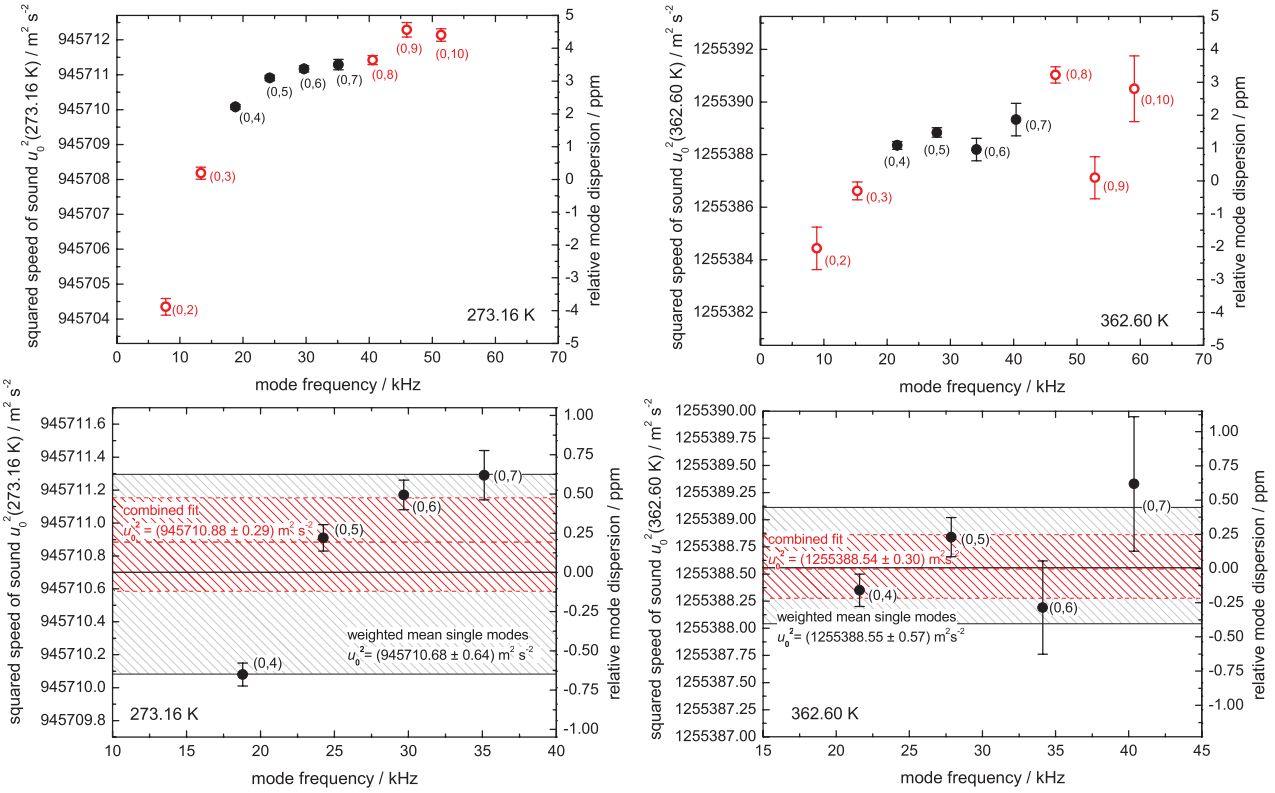

Figure 13. Squared speed of sound at zero pressure $u_0^2(T)$ for two isotherms at 273.16 K and 362.60 K. The upper graphs show the systematic dispersion of $u_0^2(T)_N$ resulting from fitting acoustic data to equation (7) for nine radial modes with error bars displaying the fitting uncertainty of each mode. The radial modes (0,4) to (0,7)—black full symbols—were selected for the final determination of $u_0^2(T)$. For these modes, the lower graphs compare the value of $u_0^2(T)$ estimated by two alternative procedures, namely a combined fit to all modes (red dashed lines) and weighted mean of single mode fits (solid black lines). Striped areas delimit the uncertainty of these estimates.

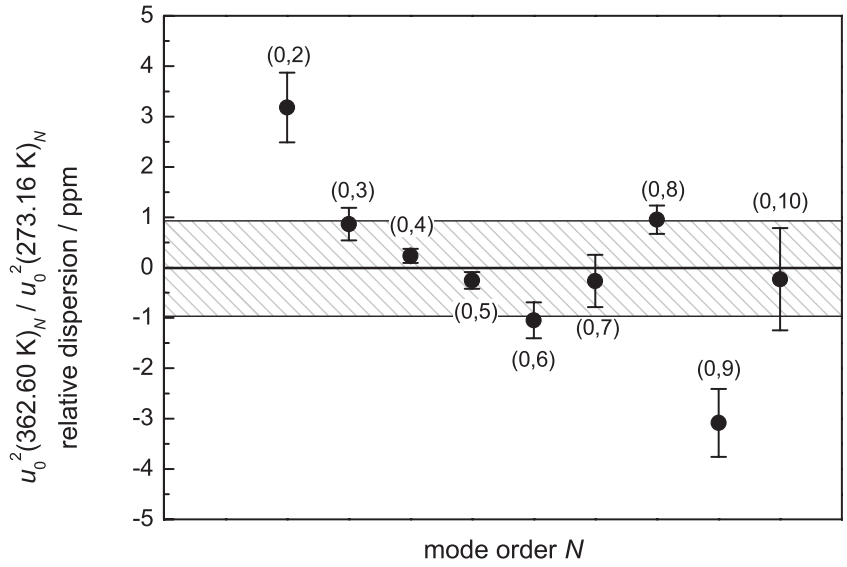

Figure 14. Relative differences between the squared speed of sound ratios $[u_0^2(T)_N/u_0^2(T_{TPW})_N]$ of individual radial modes and the ratio $\langle u_0^2(T)\rangle/\langle u_0^2(T_{TPW})\rangle$ obtained by combining the weighted mean of four selected modes at two temperatures. The striped area and the solid lines display the uncertainty of the weighted mean estimate.

twice in table 6, labeled as *mode inconsistency*, in row 1 for isotherms at T, and in row 2 for the reference isotherms at T_{TPW}.

We tested the adequateness of this particular approach to the determination of the ratio $u_0^2(T)/u_0^2(T_{TPW})$ and the estimate of its uncertainty by considering two alternative procedures.

The first alternative combines the $u^2(p, T)_N$ data for the selected modes in a single set before fitting to zero-pressure using equation (7) leading to a fitted estimate $u_0^2(T)$ that was always (i.e. for all isotherms) found consistent with that evaluated as the weighted mean of individual mode fits, with relative differences which are always less than 0.5 ppm. However,

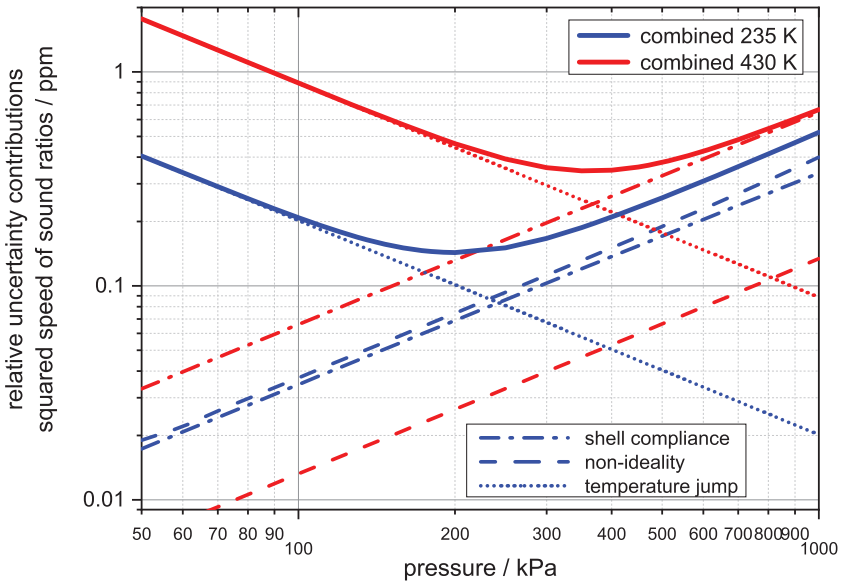

Figure 15. Relevant uncertainty contributions of a determination of T/T_{TPW} using the *single states* method at $T = 235\,\mathrm{K}$ (blue curves) and $T = 430\,\mathrm{K}$ (red curves). The dashed lines show the contribution of the calculated non-ideality of He. The dotted lines show the contribution of the temperature-jump correction. The dash-dotted lines show the contribution of the shell correction for mode (0,4) which is the nearest to the breathing frequency of the shell among those selected for the analysis (see section 4.2.2).

the uncertainty of this combined fit (figure 13) was found too small to realistically account for the dispersion of the individual modes.

As a second alternative, we used the results of the individual fits to combine the ratios $u_0^2(T)_N/u_0^2(T_{\mathrm{TPW}})_N$ mode by mode (figure 14), expecting that the systematic perturbation affecting each mode would be only weakly temperature-dependent and as such would be partially canceled out in each individual ratio. In fact, we found that the mean estimate $(1/N)\sum_N[u_0^2(T)_N/u_0^2(T_{\mathrm{TPW}})_N]$, which includes the (0,3) and (0,8) mode data in the selected set, to be consistent with the other procedures discussed above, with a maximum relative difference of 0.7 ppm or 0.5 times their combined standard uncertainty in the worst case. Such slight sensitivity of the ratio $u_0^2(T)/u_0^2(T_{\mathrm{TPW}})$ to the particular recipe used to evaluate it and to the number of modes included in the evaluation is reassuring with regard to the robustness of our evaluation of T/T_{TPW}.

We now consider the excess halfwidths, previously discussed in section 4.2 and illustrated in figure 8, and assume that the relative difference of their values at T and at T_{TPW} is a plausible estimator of the possible variation with temperature of any unmodeled frequency perturbation. We account for this possible error source with a dedicated uncertainty contribution evaluated as the mean variation, between T_{TPW} and T, for the four selected modes (0,4) to (0,7) of the relative difference $2 \times |\Delta g_N(T) - \Delta g_N(T_{\mathrm{TPW}})|/f_N$, as listed in row 3 of table 6.

In row 4 of table 6 we list the uncertainty contribution due to our imperfect estimate of the temperature jump coefficient $\zeta_{\mathrm{T}} = (6.67 \pm 0.42)$ previously discussed in section 4.2.1. To evaluate this contribution, we recorded the relative variation of $u_0^2(T)/u_0^2(T_{\mathrm{TPW}})$ upon applying the temperature-jump frequency corrections defined in [38] at both T and T_{TPW} by using the mean estimate $\zeta_{\mathrm{T}} = 6.67$ or, alternatively, the upper-limit $\zeta_{\mathrm{T}} = (6.67 + 0.42) = 7.09$ before fitting the isotherm data using equation (7).

Following the discussion in section 3.2, the uncertainty contribution of an imperfect estimate of the experimental pressure error was estimated by applying a constant offset of -10 Pa and $+10$ Pa to our experimental pressure records at T_{TPW} and T respectively before repeating the calculation of the boundary layer corrections and the final fitting procedures to our acoustic data. These repetitions resulted in relative variations of the squared ratios $u_0^2(T)/u_0^2(T_{\mathrm{TPW}})$ by the amount reported in row 5 of table 6.

Finally, the list of uncertainty contributions in table 6 is completed by two entries to respectively account for the total relative uncertainty of the squared thermal expansion of the resonator $a_0^2(T)/a_0^2(T_{\mathrm{TPW}})$, previously discussed in section 3.2, and for the possible variation of the molar mass of the He samples, which is discussed below in section 5.

4.4. Single states method: results and uncertainty budget

In this section we discuss the determination of the ratio T/T_{TPW} from the squared speed of sound ratio $u^2(p_T, T)/u^2(p_{\mathrm{TPW}}, T_{\mathrm{TPW}})$ using the *single states* method described by equation (6), where p_T and p_{TPW} are not necessarily the same and the correction from $u^2(p_x, T)$ to $u_0^2(T)$ is based on a theoretical estimate of the acoustic virial coefficients of He. To drive our particular choice of p_x, we take into account the combined effect of three uncertainty sources which are relevant to the use of this method, namely the correction to account for the non-ideality of He [9, 10] and our mean estimates of the temperature jump coefficient $\zeta_{\mathrm{T}} = (6.67 \pm 0.42)$ and the adiabatic compressibility of the shell $\chi_{\mathrm{S}} = (6.46 \pm 0.22) \times 10^{-11}\ \mathrm{Pa}^{-1}$. We observe that: the uncertainty contribution of the temperature jump correction increases both at

Table 7. Uncertainty budget for the determination of the thermodynamic temperature $T = 273.16 \times u_0^2(T)/u_0^2(T_{\mathrm{TPW}})$—*single states* method.

Date T isotherm		May 2014	Aug 2014	May 2014	Apr 2014	Jul 2014	May 2016	Jun 2016	Jun 2016	Jun 2016	Aug 2016	Aug 2016
Reference TPW isotherm		I Feb 2014	II Jul 2014	I Feb 2014	I Feb 2014	II Jul 2014	III Mar 2016	III Mar 2016	III Mar 2016	III Mar 2016	III Mar 2016	III Mar 2016
Isotherm temperature/K		235.14	236.62	247.00	260.12	302.91	334.17	334.17	362.60	395.90	396.20	430.00
Row	Uncertainty source	Relative uncertainty $u_{\mathrm{r}}(T)$/ppm										
1	Mode inconsistency at T	1.28	0.15	0.54	0.31	0.47	0.51	0.59	0.44	0.70	0.32	1.24
2	Mode inconsistency at T_{TPW}	0.41	0.47	0.41	0.41	0.47	0.49	0.49	0.49	0.49	0.49	0.49
3	Non-ideality of He and pressure	0.31	0.31	0.30	0.29	0.26	0.25	0.25	0.24	0.23	0.23	0.23
4	Excess halfwidth variation between T and T_{TPW}	0.49	0.34	0.28	0.21	0.23	0.35	0.45	0.10	0.33	0.39	0.97
5	Thermal accommodation	0.06	0.06	0.04	0.02	0.05	0.10	0.10	0.14	0.19	0.19	0.25
6	Shell perturbation	0.46	0.46	0.46	0.46	0.46	0.46	0.46	0.46	0.46	0.46	0.46
7	Thermal expansion microwave determination	0.03	0.02	0.03	0.02	0.02	0.04	0.09	0.08	0.09	0.10	0.12
8	Molar mass	0.33	0.35	0.33	0.33	0.00	0.05	0.05	0.05	0.05	0.05	0.14
	Combined/ppm	**1.57**	**0.89**	**0.98**	**0.84**	**0.88**	**0.95**	**1.04**	**0.86**	**1.07**	**0.90**	**1.75**
		relative uncertainty $u_{\mathrm{r}}(T)$/mK										
	Combined/mK	**0.37**	**0.22**	**0.25**	**0.22**	**0.26**	**0.30**	**0.34**	**0.29**	**0.40**	**0.33**	**0.74**

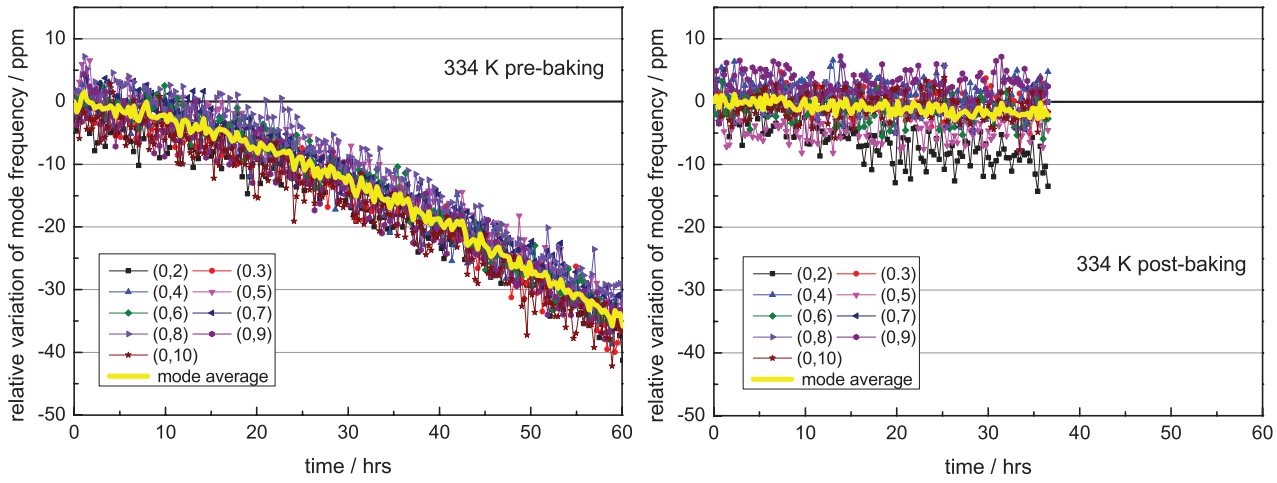

Figure 16. Relative variation of the resonance frequency of several acoustic modes recorded as a function of time at 170 kPa, 334 K before (left) and after (right) baking the cavity under vacuum at 450 K for one week. In both plots the records start at the instant $t = 0$ when the flow was stopped.

Table 8. Acoustic comparison of molar mass ratios of several He samples.

Isotherm temperature T_{90}/K	Sample used at T	Sample used at T_{TPW}	(M_T/M_{TPW}) – 1 ppm	$u_{\mathrm{r}}(M_{\mathrm{T}}/M_{\mathrm{TPW}})$ ppm	Thermodynamic condition of the acoustic estimate of M_T/M_{TPW}
235.14	MG2	MG1	−0.31	0.33	105 kPa, 273.16 K
247.00					
260.12					
302.91		MG3	—	—	—
236.62	MG4	MG3	0.21	0.35	105 kPa, 302.91 K
334.17	R6	R5	−0.06	0.05	690 kPa, 334.17 K
334.17					
362.60					
395.90					
396.20					
430.24	MG7	R5	−0.40	0.14	690 kPa, 395 K

low pressure, proportionally to p^{-1}, because of the increase in the mean free path, and at high temperature because of the increase of the thermal conductivity; the uncertainty of the non-ideality correction increases with increasing density; the uncertainty contribution of the relevant shell parameters, like the *breathing* frequency and the adiabatic compressibility of the shell, increases proportionally to pressure. The effect of the propagation of the uncertainty of these sources onto the ratio $u^2(p_T, T)/u^2(p_{\mathrm{TPW}}, T_{\mathrm{TPW}})$ were numerically calculated and are separately plotted for $T = 235$ K and $T = 430$ K, as a function of p_x, in figure 15.

The calculation assumes $p_x = p_{\mathrm{T}} = p_{\mathrm{TPW}}$, a convenient choice to minimize the additional uncertainty brought by possible calibration error of the pressure transducer. The location of the minimum of the combined uncertainties from these sources, displayed in figure 15, identifies an optimum range of pressures for implementing the *single states* method which is slightly temperature-dependent, varying between approximately 200 kPa at 235 K and 350 kPa at 430 K. Within these optimum pressure ranges we selected the values of p_x at both T and T_{TPW} to be as close as possible, typically 350 kPa or 380 kPa (see list in table 4), depending on the data available for each isotherm. We tested the impact of a different choice, with p_{T} for instance equal to 350 kPa and p_{TPW} variable between 140 kPa and 200 kPa, finding that the determination of T/T_{TPW} changed by 0.4 ppm, or equivalently less than 0.5 standard deviations, in the worst case.

The uncertainty budget for our determination of T/T_{TPW} using the *single states* method is reported in table 7.

In row 1 and row 2 of table 7, for T and T_{TPW} respectively, the listed entries correspond to half of the maximum relative dispersion of $(u_0^2)_{0N}$ determined from four selected modes, (0,4) to (0,7).

In row 3 of table 7, we list the uncertainty contribution of the correction to zero pressure of the squared speed of sound measured at (p_1, T) and $(p_{\mathrm{TPW}}, T_{\mathrm{TPW}})$. The evaluation of this contribution is based on the uncertainty estimate of the second and third acoustic virial coefficients $\beta_{\mathrm{a}}(T)$ and $\gamma_{\mathrm{a}}(T)$ [9, 10] used to prepare the corresponding plots in figure 15. Additionally, the values listed in row 3 of table 7 were evaluated accounting for a 50 ppm contribution from our imperfect determination of the gas pressure.

We next considered the possible unmodeled frequency perturbations, suggested by the disagreement between the calculated and excess halfwidths, and their possible variation between T and T_{TPW}. We account for this possibility using

Table 9. Budget of relevant uncertainty contributions to the determination of T_{90} deriving from thermometry.

Temperature/K		235.14	236.619	247.00	260.12	302.9146	334.12	334.12	362.60	395.90	396.20	430.00
Row	Uncertainty source	Relative uncertainty $u_r(T_{90})$/ppm										
1	Thermal gradient at T	0.21	0.17	0.16	0.08	0.66	0.54	0.57	0.66	0.71	0.93	1.02
2	Thermal gradient at T_{TPW}	0.11	0.29	0.11	0.11	0.29	0.04	0.04	0.04	0.04	0.04	0.04
3	Non-uniqueness type 1 sub-range inconsistency	0.00	0.00	0.04	0.04	0.00	0.00	0.00	0.00	0.00	0.00	0.00
4	Non-uniqueness type 3 platinum properties	0.00	0.01	0.19	0.41	0.00	0.26	0.26	0.25	0.16	0.16	0.00
5	Resistance measurement including bridge non-linearity	0.04	0.04	0.04	0.04	0.03	0.03	0.03	0.03	0.03	0.03	0.02
6	Fixed points including repeatability	1.11	1.10	0.61	0.34	0.23	0.45	0.45	0.58	0.83	0.88	0.93
7	Stability of cSPRTs between successive calibration	0.13	0.13	0.08	0.04	0.03	0.12	0.12	0.19	0.25	0.25	0.30
	Combined/ppm	**1.14**	**1.16**	**0.67**	**0.55**	**0.76**	**0.76**	**0.78**	**0.94**	**1.13**	**1.32**	**1.42**
		Relative uncertainty $u_r(T_{90})$/mK										
	Combined/mK	**0.27**	**0.28**	**0.17**	**0.13**	**0.23**	**0.25**	**0.26**	**0.34**	**0.43**	**0.52**	**0.61**

the mean of the relative differences $2 \times |\Delta g_N(p_1, T) - \Delta g_N(p_{TPW}, T_{TPW})|/f_N$ calculated mode by mode and listed in row 4 of table 7.

The uncertainty contribution due to our estimate of the temperature jump coefficient $\zeta_T = (6.67 \pm 0.42)$ is listed in row 5 of table 7, evaluated as $2 \times |\Delta f/f_{(p,T)} - \Delta f/f_{(p,TPW)}|$, where Δf is the thermal accommodation contribution to the boundary layer perturbation of the acoustic frequencies.

Differently from the *isotherms* method which, due to zero pressure extrapolation, is not affected by the uncertainty contribution of the shell correction, in implementing the *single states* method, only the acoustic data recorded at (p_1, T) and (p_{TPW}, T_{TPW}) are available for analysis. These data are not sufficient for a determination of the relevant shell parameters. Therefore, we calculated the shell corrections at (p_1, T) and (p_{TPW}, T_{TPW}) using the simplified model described by equation (13) and tabulated values of the mechanical properties of copper [24] as input data for this model. We do not know how to rigorously estimate the uncertainty of this approach, thus we evaluated the variation in the determination of the ratio T/T_{TPW} caused by alternatively applying, at both temperatures, shell corrections based on the model calculation or, alternatively, based on the fitted shell parameters obtained by fitting isotherms data (section 4.2.2). Depending on T, the amount of the resulting change was found to be highly variable, with a minimum of 0.02 ppm at 334.17 K and a maximum of −0.92 ppm at 396.2 K. The mean of the absolute value of these relative variations is 0.46 ppm, which is finally assumed (row 6, table 7) as a reasonable guess, equal at all temperatures, of the uncertainty contribution of the shell correction.

With the same contributions previously listed for the *isotherms* method, in row 7 and row 8 of table 7 we account for the uncertainty affecting the estimated thermal expansion of the resonator $a_0^2(T)/a_0^2(T_{TPW})$ and the estimated molar mass of the He samples used in this work.

5. Molar mass of helium samples

Differently from absolute AGT, which requires a determination of the molar mass of the thermometric gas, and may imply a determination of the isotopic abundances for most accurate work, the relative AGT implemented here has the less stringent requirement that the composition of the gas should not appreciably change between measurements at T_{TPW} and T. Among the causes of such variation, a temperature-dependent rate of desorbed impurities from the internal cavity surface and changes of the composition among different commercial samples are most plausible and were investigated by dedicated tests, as discussed in the following paragraphs.

5.1. Estimates of outgassing rates

For all the acoustic measurements reported in this work, helium gas was maintained flowing through the cavity at the constant rate of 7.5×10^{-5} mol s^{-1}, equivalent to 100 sccm. Previously reported tests at variable flow-rates [21] reassured with regard to the possible induction of relevant thermal gradients within the gas inside the cavity. Flowing at a rate of 100 sccm previously proved to be effective [21] in maintaining the contamination by outgassing and possible virtual leaks in

the apparatus at an acceptable level, at least when working near 273 K. The higher temperature range examined in this work caused concern with regard to the possible variability of the rate of outgassing. This possibility was first investigated at 170 kPa, after completing measurements along an isotherm near 334 K, by stopping the flow and observing the variation of the acoustic mode frequencies recorded as a function of time t. The plot on the left side of figure 16 illustrates such a record over a period of 2.5 d, when a relative frequency variation $1/f\ (\mathrm{d}f/\mathrm{d}t) = -14$ ppm d^{-1} was observed, a rate ten times larger than previously observed at 273.16 K [21]. In an attempt to reduce this effect, the resonator and its containing vessel were evacuated and baked at temperatures up to 450 K for one week. Acoustic measurements were then repeated along an isotherm near 334 K, and the relative variation of the acoustic modes at 170 kPa recorded one more time (figure 16) and found to have significantly decreased to -1.3 ppm d^{-1}.

Assuming that the desorption of water vapor would be mainly responsible for the observed frequency change, the corresponding outgassing rates before and after the baking procedure correspond to 2.0×10^{-10} mol m^{-2} s^{-1} and 1.8×10^{-11} mol m^{-2} s^{-1}, respectively. In a typical experimental condition, i.e. while the resonator is continuously flushed with helium at 170 kPa and at a flow rate of 100 sccm, the corresponding concentrations of water x_{H2O} in He, based on a coarse estimate of the total metal surface exposed to the gas, would be 0.4 ppm and 0.04 ppm respectively before and after baking, with a resulting relative change of the squared speed of sound in He at 170 kPa by 1.6 ppm and 0.16 ppm. If the outgassing rate remained constant at all pressures, its effect on the sample composition would increase proportionally to p^{-1}, and should affect the estimated temperature jump coefficient ζ_{T}. This is not evident (figure 9) by comparing the two estimates of $\zeta_{334\mathrm{K}}$ before and after baking. However, if the baking procedure just reduced the thickness of a water layer adsorbed on the resonator surface the quantitative effect on ζ_{T} would be hard to predict [38]. The apparatus was again baked at 450 K for 14 d, after completing measurements along an isotherm near 396 K. The relative variations of the acoustic frequencies observed before and after baking, with the cavity isolated at 170 kPa in a no-flow condition, were -24 ppm d^{-1} and -6 ppm d^{-1}, respectively. A comparison of the two fitted estimates of u_0^2 at 334 K and the two fitted estimates of u_0^2 near 396 K showed a relative increase after baking by 0.76 ppm at 334 K and 1.29 ppm at 396 K, consistent with samples of He of increased purity. These small differences, and the relevant change of the observed outgassing rates, are reassuring with respect to the possible effect of the residual contamination which might affect the purity of the thermometric gas after outgassing. The $(T - T_{90})$ results from the contaminated isotherms were not included in the recommended list in table 1.

5.2. Comparison of speed of sound in different helium samples

Due to continuous purging at 100 sccm, the consumption of helium gas necessary to complete the acoustic measurements reported in this work was significant, in the order of 50 m^3, corresponding to a total of seven cylinders purchased throughout a period of several years from two different manufacturers, respectively labeled MG and R below. The purity of the helium within all these cylinders, as declared by the manufacturer, was 99.9999 %. The He samples were further purified from chemically reactive impurities by flowing through a SAES PS2GC50- R heated getter before being admitted into the resonator.

With a single exception at the Ga point, the gaseous samples were not taken from the same bottled source at both T_{TPW} and T. Thus, in order to estimate the possible variation M_T/M_{TPW} of the molar mass due to slight differences of the ^{3}He/^{4}He ratio or trace contamination from other noble gases, upon each substitution of an exhausted bottle of He, we compared the squared acoustic frequencies at the same pressure, temperature and flow rate of a recent measurement with the previous sample. From the results of these comparisons, listed in table 8, we determined correction factors for the squared speed of sound ratios. The uncertainty of these corrections, which contributes to the overall uncertainty of $u_0^2(T)/u_0^2(T_{\mathrm{TPW}})$ and is listed as the molar mass relative uncertainty in row 7 of table 6 and row 8 of table 7 varied considerably, depending from the S/N ratio of the acoustic measurements and the gas density at which the comparison was carried out.

6. Determination of T_{90}

The methods and the instrumentation used to estimate T_{90} between 234 K and 430 K, as needed for the sake of their comparison to the acoustic determinations of the thermodynamic temperature T, were the same used in a recent determination of R and have been previously reported [21]. In the following, we update the results of the fixed-points calibrations used to link the thermometry in our laboratory to ITS-90. The combined estimated uncertainty of our T_{90} measurements varies between a minimum of 0.13 mK, relatively equivalent to 0.55 ppm, at 260 K, and a maximum of 0.61 mK (1.42 ppm) at 430 K, with contributions from several sources, as reported in table 9 and discussed below.

6.1. Temperature uniformity of the resonator

Three capsule-type standard platinum resistance thermometers (cSPRTs), manufactured by Hart Scientific, model 5686, dubbed HS156, HS157 and HS124 were used. The latter was custom designed to have a reduced length of 35 mm and filled with a oxygen/argon mixture instead of helium to increase long-term stability. The thermometers were placed in thermal contact with the resonator at different locations, respectively at the top and bottom ends of the cavity and, in one case more laterally, close to the equatorial flange. This spatial distribution was intended to evidence any vertical and/or horizontal temperature gradient across the cavity. The temperature of the gas in the resonator was calculated from the average of the readings of the three cSPRTs. The differences between these readings varied as a function of temperature and depending on the position of the cSPRTs. The differences were found to be

minimal, typically less than 0.1 mK, when measuring near the triple point of water (TPW). However, when measuring below and above the ambient temperature T_{amb}, temperature differences were observed to increase in proportion to $|T - T_{amb}|$. At all temperatures below T_{amb}, the thermometer located in the bottom of the cavity was warmer than those embedded at the equator and the top, with a maximum recorded difference of 0.17 mK at 235 K. At all temperatures above T_{amb}, the sign of the temperature difference was reversed with the bottom cSPRTs indicating the lowest temperature and, in most cases, the cSPRT at the equator was found slightly warmer than that located at the top; at 430 K the measured temperature difference between the equator and the bottom part of the resonator was 1.52 mK (see electronic supplement[9] for details). We have no satisfactory explanation for these observed temperature differences, which are opposite in sign from those expected as a consequence of heat conduction between the laboratory to the top of the resonator. The differences could possibly be related to temperature stratification of the liquid bath surrounding the pressure vessel. Unfortunately, the temperature of the bath was measured at just one position with an industrial PT100 thermometer for the main sake to maintain it stable using a heater, and these data were not recorded.

It is worth observing that, in spite of their relevance, the observed temperature gradients do not affect, at any appreciable level, the determination of the thermodynamic temperature T which depends on the average speed of sound in the cavity [44]. It appears then appropriate to ascribe this contribution in the uncertainty budget of T_{90}, as reported in row 1 and row 2 of table 9 where, assuming a range of uniform probability for the readings of the three cSPRTs, the listed entries are the maximum recorded difference between any couple of cSPRTs divided by a factor $2\sqrt{3}$.

6.2. Fixed points calibration and thermometers stability

During the two-years course of this work, a historical record of the stability of the cSPRTs at the TPW was periodically updated to evidence any variation of their resistance at the TPW which might occur following relevant temperature excursions. The maximum recorded variations was −0.33 mK for one cSPRT, +0.12 mK for another, and within 0.03 mK for the third. Stability at the TPW was an important requisite for the sake of an accurate determination of the Boltzmann constant, but is not affecting T_{90} determinations obtained by relative AGT where only the stability of $W = R(T)/R(273.16\,\mathrm{K})$ matters, as it is further commented below.

All three cSPRTs were calibrated at the INRiM facility maintaining the ITS-90 fixed points for long-stem SPRTs [45]. For that purpose the cSPRTs were mounted, one at a time, within a copper sleeve embedded into a hollow stainless steel adaptor designed to reproduce the exterior dimensions of long-stem thermometers. At the fixed points other than indium, ethyl alcohol was used as a contact liquid within the fixed-point well and measured self-heating were found to be comparable to those typically obtained with long stem thermometers. The fixed points used for calibration were the triple point of mercury (Hg), the melting point of gallium (Ga) and the freezing point of indium (In). This choice implies two different subranges of the ITS-90 for temperature evaluation: (Hg–Ga) and (TPW-In), with a resulting contribution from sub-range inconsistency, i.e. type 1 non-uniqueness (NU1), whose evaluation was performed based on the *Guide to the Realization of the ITS-90: Platinum Thermometry* [46]. For the temperature range below 0 °C, equation (55) with the coefficients in table 5 of [46] was used, while for the temperature range (Hg–Ga) equation (54) in [46] was adapted for the overlap between (TPW-Ga) and (TPW-In), as an estimated guess for NU1 in this range; since cSPRTs are rarely calibrated at temperatures above the tin point—in order not to compromise the glass seal causing gas leaks—this contribution is considered to be nil for temperatures in the range (Ga–In). These evaluations resulted in a uncertainty contribution, listed in row 3 in table 9, always lower than 0.01 mK.

An additional uncertainty contribution is given by type 3 non-uniqueness (NU3). This type of non-uniqueness deals with the fact that SPRTs, being artefacts, are imperfect interpolating devices. This means that, assuming zero uncertainty for the fixed-point calibrations, different SPRTs calibrated at the *same* fixed-points produce slightly different temperature values between the fixed points. The values reported for this contribution in row 4 of table 9 were calculated with the equations given in table 6 of [46] for the temperature range below 0 °C and with the equations of table 7 therein for the temperature range above 0 °C.

In row 5 of table 9, the contribution denominated ‘resistance measurement’ accounts for the estimated non-linearity of the F18 resistance bridge, the uncertainty of extrapolating to zero current (self-heating), and the effect of slight temperature variations of the standard resistor.

Full-range calibrations at Hg, TPW, Ga and In were performed in December 2013 and December 2014, after completing a subset of the measurements reported in this work. An additional calibration was performed in February 2016, limited to the subrange (TPW-In).

In row 6 of table 9, we list the uncertainty related to the realization of the fixed points maintained at INRiM, which is well characterized from international comparisons. These uncertainties are propagated to temperatures which are intermediate between fixed points, resulting in contributions between 0.07 mK at Ga and 0.4 mK at In.

Finally, in row 7 of table 9, we use the full calibration history of the cSPRTs to estimate their stability, and account for their possible variation between successive calibrations. These contributions were estimated considering half of the maximum variation recorded for each cSPRT, averaging to a single mean value for the set, multiplying by 1/3 to account for its effect on the average temperature of the gas and, finally by linearly interpolating between the fixed points.

7. Concluding remarks

The present determinations of the thermodynamic temperature T, derived from measurement of the speed of sound in He between 236 K and 430 K, have relative uncertainties between

[9] See footnote 2.

0.7 ppm and 1.6 ppm which are comparable to the uncertainty of their approximation T_{90} by the International Temperature Scale of 1990. The corresponding determinations of $(T - T_{90})$ are found remarkably consistent with other recent results obtained by AGT, within the low combined uncertainties and in spite of the use of He instead of Ar.

In addition to extrapolating to zero pressure the speed of sound measured along isotherms, we considered an alternative procedure of analysis of our acoustic data which corrects the acoustic non-ideality using *ab initio* calculations of the density and the acoustic virial coefficients of He. We find that this alternative approach leads to determinations of T which are consistent with the isotherm analysis. Looking ahead the possible future utilization of AGT for the direct calibration of thermometers on the thermodynamic temperature scale, speed of sound measurements at a single thermodynamic state would be preferable because less time-consuming, by approximately a factor of five, compared to the duration of a complete isotherm record.

The uncertainty budget of both methods (see tables 6 and 7) indicates that the major contribution is the inconsistency among different acoustic modes, likely as a consequence of our limited capability to predict the perturbations induced by the finite mechanical admittance of the resonator wall. Particularly, the perturbations arising from the elastic recoil of the cavity shell are hard to estimate and, for the *single states* method, bring an additional contribution to the uncertainty budget. To minimize these effects, cavities with an increased ratio between the shell thickness and the internal radius and increased stiffness at the wall and at the joints should be realized.

Electronic supplement

This article is combined with a supplementary section which comprises:

- Original acoustic, microwave and thermometry records for 14 isotherms, with separate records for each pressure considered along each isotherm;
- tabulated lists of the corrections applied to account for the relevant perturbations to the acoustic and microwave frequencies; averaged, corrected isotherm data used to extrapolate, by fitting, zero-pressure values of the squared speed of sound and the cavity radius;
- historical records of the calibration results of each SPRT and estimated resistance ratios $W(T) = R(T)/\mathrm{R}(T_{\mathrm{TPW}})$ for each SPRT, where T is the thermodynamic temperature;
- summary tables displaying for both acoustic and microwave isotherm data the results and the uncertainty of isotherm fits to zero pressure,

allowing the interested reader to reproduce and check all the analysis which leads from the original raw data to the final $(T–T_{90})$ results.

Acknowledgments

This work was carried out within the projects "Implementing the new Kelvin-InK" and "Implementing the new Kelvin 2-InK2. These projects (SIB01 InK) and (15SIB02 InK 2) have received funding from the EMRP and EMPIR programmes co-financed by the Participating States and from the European Union's Horizon 2020 research and innovation programme.

ORCID iDs

R M Gavioso https://orcid.org/0000-0002-1631-5133
D Madonna Ripa https://orcid.org/0000-0002-8760-8574
P P M Steur https://orcid.org/0000-0001-5161-8554
D Imbraguglio https://orcid.org/0000-0002-1289-772X

References

[1] Preston-Thomas H 1990 The international temperature scale of 1990 (ITS-90) *Metrologia* **27** 3–10
[2] Fischer J *et al* 2011 Present estimates of the differences between thermodynamic temperatures and the ITS-90 *Int. J. Thermophys.* **32** 12–25
[3] Gavioso R M *et al* 2016 Progress towards the determination of thermodynamic temperature with ultra-low uncertainty *Phil. Trans. R. Soc.* A **374** 20150046
[4] Moldover M R, Gavioso R M, Mehl J B, Pitre L, de Podesta M and Zhang J T 2014 Acoustic gas thermometry *Metrologia* **51** R1–19
[5] Gaiser C, Zandt T and Fellmuth B 2015 Dielectric constant gas thermometry *Metrologia* **52** S217–26
[6] Qu J, Benz S P, Coakley K, Rogalla H, Tew W L, White R, Zhou K and Zhou Z 2017 An improved electronic determination of the Boltzmann constant by Johnson noise thermometry *Metrologia* **54** 549–58
[7] Mohr P J, Newell D B, Taylor B N and Tiesinga E 2018 Data and analysis for the CODATA 2017 special fundamental constants adjustment *Metrologia* **55** 125–46
[8] CPGM 2018 *Resolution 1 of the 26th CGPM* (www.bipm.org/en/CGPM/db/26/1/)
[9] Cencek W, Przybytek M, Komasa J, Mehl J B, Jeziorski B and Szalewicz K 2012 Effects of adiabatic, relativistic, and quantum electrodynamics interactions on the pair potential and thermophysical properties of helium *J. Chem. Phys.* **136** 224303
[10] Garberoglio G, Moldover M R and Harvey A H 2011 Improved first principles calculation of the third virial coefficient of helium *J. Res. Natl Inst. Stand. Technol.* **116** 729–42
[11] Gaiser C, Fellmuth B and Haft N 2017 Primary thermometry from 2.5 K to 140 K applying dielectric-constant gas thermometry *Metrologia* **54** 141–7
[12] Rourke P M C 2017 NRC microwave refractive index gas thermometry implementation between 24.5 K and 84 K *Int. J. Thermophys.* **38** 107
[13] Underwood R, de Podesta M, Sutton G, Stanger L, Rusby R, Harris P, Morantz P and Machin G 2016 Estimates of the difference between thermodynamic temperature and the International Temperature Scale of 1990 in the range 118 K to 303 K *Phil. Trans. R. Soc.* A **374** 20150048
[14] Underwood R, de Podesta M, Sutton G, Stanger L, Rusby R, Harris P, Morantz P and Machin G 2017 Further estimates of $(T - T_{90})$ close to the triple point of water *Int. J. Thermophys.* **38** 44
[15] Moldover M R, Boyes S J, Meyer C W and Goodwin A R H 1999 Thermodynamic temperatures of the triple points of mercury and gallium and in the interval 217 K to 303 K *J. Res. Natl Inst. Stand. Technol.* **104** 11–46

[16] Strouse G F, Defibaugh D R, Moldover M R and Ripple D C 2003 Progress in primary acoustic thermometry at NIST: 273K to 505K *Temperature: its measurement and control in science and industry* vol VII *8th Int. Temperature Symp. (Chicago, IL, 21–24 October 2002)* ed D C Ripple (New York: AIP) pp 31–6
[17] Ripple D C, Strouse G F and Moldover M R 2007 Acoustic thermometry results from 271 K to 552 K *Int. J. Thermophys.* **28** 1789–99
[18] Ewing M B and Trusler J P M 2000 Primary acoustic thermometry between $T = 90$ K and $T = 300$ K *J. Chem. Thermodyn.* **32** 1229–55
[19] Benedetto G, Gavioso R M, Spagnolo R, Marcarino P and Merlone A 2004 Acoustic measurements of the thermodynamic temperature between the triple point of mercury and 380 K *Metrologia* **41** 74–98
[20] Pitre L, Moldover M R and Tew W L 2006 Acoustic thermometry: new results from 273 K to 77 K and progress towards 4 K *Metrologia* **43** 142–62
[21] Gavioso R M, Madonna Ripa D, Steur P P M, Gaiser C, Truong D, Guianvarc'h C, Tarizzo P, Stuart F M and Dematteis R 2015 A determination of the molar gas constant R by acoustic thermometry in helium *Metrologia* **52** S274–304
[22] Matula R A 1979 Electrical resistivity of copper, gold, palladium, and silver *J. Phys. Chem. Ref. Data* **8** 1147–298
[23] May E F, Pitre L, Mehl J B, Moldover M R and Schmidt J W 2004 Quasi-spherical resonators for metrology based on the relative dielectric permittivity of gases *Rev. Sci. Instrum.* **75** 3307–17
[24] Simon N J, Drexler E S and Reed R P 1992 *NIST Monograph 177—Properties of Copper and Copper Alloys at Cryogenic Temperatures* (Boulder, Co: National Institute of Standards and Technology)
[25] Puchalski M, Piszczatowski K, Komasa J and Jeziorski B 2016 Theoretical determination of the polarizability dispersion and the refractive index of helium *Phys. Rev.* A **93** 032515
[26] Bruch L W and Weinhold F 2000 Diamagnetism of helium *J. Chem Phys.* **113** 8667–70
[27] Rizzo A, Hättig C, Fernandez B and Koch H 2002 The effect of intermolecular interactions on the electric properties of helium and argon: III. Quantum statistical calculations of the dielectric second virial coefficients *J. Chem. Phys.* **117** 2609–18
[28] de Podesta M, Underwood R, Sutton G, Morantz P, Harris P, Mark D F, Stuart F M, Vargha G and Machin G 2013 A low-uncertainty measurement of the Boltzmann constant *Metrologia* **50** 354–76
[29] Pitre L, Sparasci F, Truong D, Guillou A, Risegari L and Himbert M E 2011 Measurement of the Boltzmann constant k_B using a quasi-spherical acoustic resonator *Int. J. Thermophys.* **32** 1825–86
[30] Mehl J B 2009 Second-order electromagnetic eigenfrequencies of a triaxial ellipsoid *Metrologia* **46** 554–9
[31] Underwood R, Mehl J B, Pitre L, Edwards G, Sutton G and de Podesta M 2010 Waveguide effects on quasispherical microwave cavity resonators *Meas. Sci. Technol.* **21** 075103
[32] Moldover M R, Mehl J B and Greenspan M 1986 Gas-filled spherical resonators: theory and experiment *J. Acoust. Soc. Am.* **79** 253–72
[33] Wieser M E and Berglund M 2009 Atomic weights of the elements 2007 (IUPAC Technical Report) *Pure Appl. Chem.* **81** 2131–56
[34] Mohr P J, Newell D B and Taylor B N 2012 CODATA recommended values of the fundamental physical constants: 2010 *Rev. Mod. Phys.* **84** 1527–605
[35] Newell D B *et al* 2018 The CODATA 2017 values of h, e, k, and N_A for the revision of the SI *Metrologia* **55** L13–6
[36] Mehl J B 1985 Spherical acoustic resonator: effects of shell motion *J. Acoust. Soc. Am.* **78** 782–8
[37] Gillis K A 2012 Second-order boundary corrections to the radial acoustic eigenvalues for a spherical cavity *Metrologia* **49** L21–4
[38] Sharipov F and Moldover M R 2016 Energy accommodation coefficient extracted from acoustic resonator experiments *J. Vac. Sci. Technol.* A **34** 061604
[39] Gavioso R M, Madonna Ripa D, Guianvarc'h C, Benedetto G, Giuliano Albo P A, Cuccaro R, Pitre L and Truong D 2010 Shell perturbations of an acoustic thermometer determined from speed of sound in gas mixtures *Int. J. Thermophys.* **31** 1739–48
[40] Truong D, Sparasci F, Foltête E, Ouisse M and Pitre L 2011 Measuring shell resonances of spherical acoustic resonators *Int. J. Thermophys.* **32** 427–40
[41] Young W C and Budynas R G 2002 *Roark's Formulas for Stress and Strain* (New York: McGraw-Hill) p 685
[42] Gillis K A, Lin H and Moldover M R 2009 Perturbations from ducts on the modes of acoustic thermometers *J. Res. Natl Inst. Stand. Technol.* **114** 263–85
[43] Guianvarc'h C, Gavioso R M, Benedetto G, Pitre L and Bruneau M 2009 Characterization of condenser microphones under different environmental conditions for accurate speed of sound measurements with acoustic resonators *Rev. Sci. Instrum.* **80** 074901
[44] Gillis K A, Schmidt J W, Mehl J B and Moldover M R 2015 'Weighing' a gas with microwave and acoustic resonances *Metrologia* **52** 337–52
[45] Marcarino P, Steur P P M and Dematteis R 2003 Realization at IMGC of the ITS-90 fixed points from the argon triple point upwards, temperature, its measurement and control in science and industry *AIP Conf. Proc.* 684 65–70
[46] Consultative Committee for Thermometry (CCT) under the auspices of the International Committee for Weights and Measures 2015 *Guide to the Realization of the ITS-90: Platinum Resistance Thermometry* (www.bipm.org/en/committees/cc/cct/guide-its90.html)